Oncogenic KRAS-induces necroptotic priming of pancreatic neoplasia

Sofya Tishina
University of Cologne
Alina Dahlhaus
University of Cologne
Ariadne Androulidaki
Cologne University
Michael Kotliar
Cincinnati Children's Hospital Medical Center
Lejla Mulalic
University of Cologne
Hassan Rakhsh-Khorshid
University of Cologne
Florian Hocher
University of Kiel
Jenny Stroh
University of Cologne
Julia Beck
University of Cologne
Marta Manik
University of Cologne
Riley Williams
Fox Chase Cancer Center
Gülce Gülcüler
University of Cologne
Ali Abdallah
University of Cologne
Christina Bebber
University of Cologne https://orcid.org/0000-0002-7841-7493
Moritz Reese
University of Cologne
Jonathan Lim
https://orcid.org/0000-0002-1798-8954
Anna Trauzold

University of Kiel
Alexander Quaas
University of Cologne
Johannes Brägelmann
University of Cologne https://orcid.org/0000-0002-1306-2169
Filippo Beleggia
University of Cologne https://orcid.org/0000-0003-0234-7094
Manolis Pasparakis
University of Cologne https://orcid.org/0000-0002-9870-0966
Gianmaria Liccardi
CECAD Cluster of Excellence, University of Cologne
Siddharth Balachandran
Fox Chase Cancer Center https://orcid.org/0000-0003-2084-1803
Igor Astsaturov
igor.astsaturov@fccc.edu https://orcid.org/0000-0002-8613-1890
Silvia Von Karstedt (s.vonkarstedt@uni-koeln.de)
University of Cologne https://orcid.org/0000-0002-7816-5919

Research Article

Keywords: PDAC, KRAS, Cancer, cell death, necroptosis, caspase 8

Posted Date: July 24th, 2023

DOI: https://doi.org/10.21203/rs.3.rs-2971504/v2

Additional Declarations: There is **NO** Competing Interest.

Oncogenic KRAS-induces necroptotic priming of pancreatic neoplasia

Sofya Tishina[1, 2], Alina Dahlhaus[1, 2], Ariadne Androulidaki[1, 2], Michael Kotliar[3], Lejla Mulalic[1, 2], Hassan Rakhsh-Khorshid[4], Florian Hocher[5], Jenny Stroh[1, 2], Julia Beck[1, 2], Marta Manik[1, 2], Riley M. Willliams[6], Gülce G. Balta[1], Ali T. Abdallah[2], Christina M. Bebber[1, 2], Moritz Reese[1, 2], Jonathan K. M. Lim[7], Anna Trauzold[5, 8], Alexander Quaas[9], Johannes Brägelmann[1, 10, 11], Filippo Beleggia[1], Manolis Pasparakis[2, 11, 12], Gianmaria Liccardi[4], Siddharth Balachandran[6], Igor Astsaturov[13] & Silvia von Karstedt[1, 2, 11, #]

[1]University of Cologne, Faculty of Medicine and University Hospital Cologne, Department of Translational Genomics, Cologne, Germany.

[2]CECAD Cluster of Excellence, University of Cologne, Cologne, Germany.

[3]Cincinnati Children's Hospital Medical Center, Division of Allergy and Immunology, Cincinnati, USA

[4]University of Cologne, Faculty of Medicine and University Hospital Cologne, Center for Biochemistry, Cologne, Germany.

[5]University of Kiel, Institute for Experimental Cancer Research, Kiel, Germany

[6]Fox Chase Cancer Center, Cancer Signaling and Microenvironment Program, Philadelphia, USA

[7]Heinrich Heine University, Medical Faculty and University Hospital Düsseldorf, Institute of Neuropathology, Düsseldorf, Germany.

[8]University Hospital Schleswig-Holstein (UKSH), Department of Gynecology and Obstetrics, Campus Kiel, Kiel, Germany.

[9]University of Cologne, Faculty of Medicine and University Hospital Cologne, Institute of Pathology, Cologne, Germany.

[10]University of Cologne, Faculty of Medicine and University Hospital Cologne, Mildred Scheel School of Oncology, Cologne, Germany.

[11]University of Cologne, Faculty of Medicine and University Hospital Cologne, Center for Molecular Medicine Cologne, Cologne, Germany.

[12]University of Cologne, Institute for Genetics, Cologne, Germany

[13]Fox Chase Cancer Center, Molecular Therapeutics Program, Philadelphia, USA

[#]Corresponding author: S von Karstedt, Department of Translational Genomics/CECAD, University of Cologne, CECAD Research Building, Joseph-Stelzmann-Str. 26, 50931 Cologne, Germany. Tel.: +49 (0)221 / 478 84340; E-mail: s.vonkarstedt@uni-koeln.de

SUMMARY

Pancreatic ductal adenocarcinoma (PDAC) is a leading cause of cancer mortality. PDAC expresses high levels of caspase 8, a central enzyme controlling various types of regulated cell death. Here, using genetically engineered mouse models we find that oncogenic KRAS-driven neoplastic transformation induces a transcriptional state of necroptotic priming, but necroptosis itself is counter selected against through co-upregulation of caspase 8. Mechanistically, expression of the driver oncogene KRAS induced a STING-dependent type I interferon (IFN) response resulting in upregulation of the necroptosis pathway leading to necroptotic priming. High caspase 8 expression in precursor lesions was a result of co-selection to prevent necroptosis. Hence, genetic or pharmacological targeting of caspase 8 was therapeutically highly efficacious in models of genetically engineered PDAC *in vivo*. These results identify type I IFN-induced necroptotic priming as synthetic lethality of KRAS-driven PDAC and show that targeting it has therapeutic benefit in this incurable malignancy.

INTRODUCTION

Caspase 8 is essential for the induction of extrinsic apoptosis triggered through death receptors belonging to the tumor necrosis factor (TNF) receptor (TNFR)-superfamily [1]. Moreover, during development and in healthy adult tissue homeostasis caspase 8 protects cells from aberrant necroptosis [2–4], a non-apoptotic form of cell death driven by RIPK1, RIPK3 [5,6] and MLKL [4]. While its role in normal tissue homeostasis has been the subject of intense investigation, the role of caspase 8 in neoplastic disease remains controversial and both up- and downregulation has been observed. In cancers with neuroendocrine differentiation caspase 8 expression is characteristically low and this has been suggested to promote metastasis by disabling apoptosis [7–12]. By contrast, high nuclear caspase 8 has been shown to promote melanoma by protecting from p53-driven apoptosis [13]. Moreover, caspase 8 expression fulfils a central role in promoting liver injury- and inflammation-associated hepatocarcinogenesis [14,15]. Despite these advances, genetic evidence for a role of caspase 8 in neoplastic disease driven by defined oncogenes has been lacking. Interestingly, analyzing caspase 8 expression within the cancer genome atlas (TCGA) we found that all human cancers with frequent activating point mutations in the small GTPase KRAS highly expressed caspase 8 (Figure S1A). These included lung adenocarcinoma (LUAD), colon adenocarcinoma (COAD) and pancreatic ductal adenocarcinoma (PDAC, PAAD in TCGA). PDAC is amongst the deadliest cancer entities and it is expected to become the second leading cause of cancer-related deaths within this decade [16–18]. Interestingly, caspase 8 mRNA was also upregulated in PDAC as compared to adjacent normal pancreas in two independent patient cohorts [19,20] (Figure S1B, C) and in a recent proteogenomic study [21]. Overall, these data hint at an unrecognized cancer-beneficial function of caspase 8 expression in several cancer entities in general and in the context of oncogenic KRAS-driven neoplasia in particular.

Caspase 8 upregulation protects oncogenic KRAS-driven pancreatic neoplasia

To approach a potential causal connection of KRAS-driven neoplastic transformation and caspase 8 upregulation, we first correlated caspase 8 expression in human PDAC and normal pancreatic tissue using respective datasets from TCGA (PAAD) and the genotype tissue expression project (GTEx) with a recently published new score for transcriptional RAS pathway activation (Ras84) which provides robust means to determine Ras-pathway

transcriptional activity [22]. Indeed, caspase 8 expression strongly correlated with the Ras84 score in PDAC while normal pancreas showed significantly less caspase 8 and Ras84 score expression (Figure 1A). Of note, the few cases of neuroendocrine pancreatic cancers contained within the PAAD dataset expressed explicitly low levels of caspase 8 and Ras84. Moreover, the 10% of PDAC patients with lowest caspase 8 expression constituted a group of PDAC supersurvivors (Figure 1B). In order to genetically define the function of caspase 8 in KRAS-driven PDAC, we first addressed whether PDAC-specific caspase 8 upregulation as compared to adjacent normal pancreas was recapitulated within the most commonly used genetically engineered mouse model (GEMM). In this model, hemizygous expression of Lox-Stop-Lox (LsL)-$KRAS^{G12D}$ (K) is targeted to pancreatic precursor cells (PDX1-Cre; C) giving rise to all stages of pancreatic intraepithelial neoplasia (PanINs) and adenocarcinoma (KC-mice) [23]. In order to specifically assess mRNA expression of caspase 8 in PanINs as compared to adjacent normal pancreas, we crossed KC-mice to a reporter strain in which all tissues express tandem tomato (tdTomato) which switch to expression of green fluorescent protein (GFP) upon Cre-mediated excision ($ROSA26^{mTmG}$-mice) [24]. As expected, macroscopic pancreata showed mosaic $tdTomato^+$ and GFP^+ areas and microscopic inspection confirmed these to be mutually exclusive (Figure S1D). Next, pancreatic tissues were digested and GFP^+ and GFP^- cells were sorted by fluorescent cell sorting (Figure 1c, Figure S1E) and subjected to RNA extraction and quantitative real-time PCR (qPCR). Strikingly, GFP^+ PanIN cells expressing $KRAS^{G12D}$ from 4 individual mice expressed significantly elevated levels of caspase 8 mRNA as compared to adjacent normal tissue (Figure 1D). Next, to approach a function of caspase 8 in pancreatic tissue before and after oncogenic transformation, we first generated mice with mosaic deletion of caspase 8 in normal pancreatic precursor cells, PDX1-Cre (C);$Casp8^{FL/FL}$($C8^{FL/FL}$). Surprisingly, and unlike in other organs, C-$C8^{FL/FL}$ mice did not show any overt signs of inflammatory disease of the pancreas or changes in $CD45^+$ immune infiltrates (Figure 1E, Figure S1F). To test whether caspase 8 deletion may instead elicit an inflammatory response in the context of neoplastic transformation, we crossed $C8^{FL/FL}$ mice with KC-mice. Indeed, expression of $KRAS^{G12D}$ resulted in a drastic overall increase in $CD45^+$ immune infiltrates (Figure S1F). Strikingly, caspase 8 deletion led to a drastic amelioration of PanIN development in KC-mice with more than 60% of ducts presenting with normal morphology and only 30% of ducts presenting with low grade cytokeratin 19^+ (CK19) lesions (Figure 1E-G). Of note, caspase 8 protein was also upregulated within PanINs as compared to adjacent normal pancreas in tissue stainings of KC-mice and effectively depleted in KC-$C8^{Fl/Fl}$ lesions (Figure S1G). Importantly, relative immune infiltration was nevertheless enhanced within the fewer $CK19^+$

lesions obtained upon deletion of caspase 8 (Figure 1H) suggesting that caspase 8 deletion can revert immune exclusion, a characteristic feature observed in the majority of human PDAC cases [25]. To obtain a comprehensive characterization of immune infiltration and ductal cellular differentiation states upon caspase 8 deletion, we next analyzed the transcriptomes of single cells isolated from 5 months-old KC-pancreata with or without caspase 8 deletion. After initial quality control and pooled analysis batch correction [26], we obtained transcriptomes from 5,356 cells from KC-C8$^{WT/WT}$ (3 mice) and 8,251 cells from KC-C8$^{Fl/Fl}$ (2 mice) pancreata. Overall, dimensionality reduction using Uniform Manifold Approximation and Projection (UMAP) identified 12 cell clusters in all replicates whose cellular identity was inferred from established pancreatic lineage markers [27,28]. While pancreatic acinar, ductal, mesothelial and inflammatory cancer-associated fibroblasts (iCAFs) could be detected, a significant proportion of single cells constituted immune cells in both genotypes (Figure 1I). Importantly, within the non-immune compartment (CD45^{-} cells), highest caspase 8 expression was detected within ductal cells containing the PanIN cell fraction and was downregulated in the majority but not all caspase 8$^{Fl/Fl}$ ductal cells (Figure S2A). Ductal cells from KC-C8$^{Fl/Fl}$ mice showed significantly lower expression of the transcription factor Sox9- a known driver of acinar-to-ductal cell reprogramming [29] (Figure S2B) supporting the presence of less progressed PanINs in the absence of caspase 8. In line with the histology data (Figure S1F), the overall amount of CD45^{+} cells within the scRNA-seq dataset did not differ between KC-C8$^{WT/WT}$ and KC-C8$^{Fl/Fl}$ (30.6% in WT, 32% in FL) yet differences within individual immune cell clusters were evident from the initial UMAP analysis. In order to resolve differences within the infiltrating immune compartment, we next re-clustered CD45^{+} cells only and identified 10 distinct clusters in all samples whose cellular identity was inferred from published mouse immune cell markers for scRNA-seq data [30] (Figure S2C). Interestingly, absence of caspase 8 specifically increased the overall B-cell, and in particular plasma cell compartment, a cell type associated with anti-tumor immunity [17,31] (Figure S2D). Moreover, conventional dendritic cell (cDC1) -described to promote T-cell cross presentation and anti-tumor immunity [32]- along with T-cell cluster proportions were also increased upon caspase 8 deletion. Klf2, a transcription factor highly expressed by naïve CD8 T-cells which is downregulated in effector cytotoxic T lymphocytes [33] was expressed at significantly lower levels in the cytotoxic T- and NK-cell fraction of KC-C8$^{FL/FL}$ mice (Figure S2E). Along similar lines, expression of Malt1, a paracaspase promoting induction of NF-kB downstream of B- and T-cell receptor activation was upregulated within the cytotoxic T- and NK-cell fraction in KC-C8$^{FL/FL}$ mice (Figure S2F). Consistent with this, there was a trend towards higher levels of the T-cell effector interferon-γ (IFN-γ) along with

known NF-kB-induced chemo- and cytokines including CXCL2 (Figure 1J). Moreover, we could trace activated NK- and T-cells as the cellular source of increased IFN-γ, total T-cells as the source for IL-4 production and neutrophils/eosinophils as the main source of CXCL2 on single-cell level (Figure 1K). Differential gene expression analysis within the neutrophil/eosinophil cluster (cluster 4) indeed revealed genes associated with neutrophil activation to be highly enriched in the KC-C8$^{Fl/Fl}$ group (Figure S2G). Given that at time of sampling (5 months), KC-C8$^{Fl/Fl}$ mice had already less PanINs and some of the differential immune response might have subsided, we also profiled immune infiltrates at 3 months of age, a time at which pancreata showed minimal PanIN development in both groups (Figure S2H). Indeed, pancreata of 3 months-old KC-C8$^{Fl/Fl}$ mice contained significantly elevated level of neutrophils (CD11b+Gr1+ cells) (Figure S2I), reduced levels of M2-macrophages (Figure S2J) and enhanced levels of inflammatory chemo- cytokines indicative of innate immune activation (Figure S2K). Taken together, caspase 8 upregulation is an inherent feature of pancreatic neoplasia which serves cancer progression and protects the maintenance of an M2-type immune environment.

Pancreatic neoplasia progression is pruned by constitutive necroptosis and apoptosis

Neutrophils are known to infiltrate sites of cell death within tissues [34] in particular in the context of necroptotic cell death [35]. Given that we observed an amelioration of disease and increased neutrophil infiltration upon caspase 8 deletion within PanINs, we next tested whether the reduced disease burden observed upon caspase 8 deletion was caused by induction of necroptosis. Indeed, all non-immune cells (CD45$^-$ cells) within the pancreas expressed caspase 8, RIPK1, RIPK3, ZBP1 and MLKL fulfilling the prerequisite to undergo necroptotic cell death (Figure 2A). In addition, necroptosis can be induced by TNF-superfamily death ligand stimulation including TNF, CD95L or TRAIL all of which are known to be expressed by activated immune cells while TRAIL was also suggested to be expressed by KRAS-mutated cancer cells [36,37]. Interestingly, we found TNF to be widely expressed by innate immune cells, CD95L expression was restricted to the T- and effector cell compartment and TRAIL was in addition also expressed by endothelial and ductal cells supporting a possibility of autocrine stimulation [37] (Figure 2A). The presence of soluble death ligand protein expression could also be confirmed using ELISA on whole pancreas extracts from KC-mice (Figure S3A-C). To test whether necroptosis was responsible for disease amelioration upon caspase 8 deletion, we crossed KC-C8$^{Fl/Fl}$ mice with mice deficient in the essential necroptosis downstream effector

MLKL [38]. While the CK19^{+} area was not fully reversed due to the fact that very large ductal lesions with very thin CK19^{+} ductal linings were observed in KC-C8$^{Fl/Fl}$; MLKL$^{-/-}$ mice, MLKL deletion fully reverted the amelioration observed in pathological PanIN quantification caused by caspase 8 deletion (Figure 2B-D). Moreover, when analyzing bulk RNA samples from these mice via qPCR, we found that the increase in perforin 1, IFN-γ, CXCL10 and CXCL2 cDNA and protein level observed upon caspase 8 deletion was reverted upon MLKL co-deletion (Figure 2E, F).

While the effect on decreased PanIN progression in the absence of caspase 8 was fully reverted upon additional deletion of MLKL, upon necropsy at experimental endpoint we noted a drastically increased occurrence of macroscopic liver lesions confirmed to be liver metastasis by pathological inspection in 68% of KC-C8$^{Fl/Fl}$; MLKL$^{-/-}$ as opposed to 38,5 % in KC-C8$^{wt/wt}$ and only 28,6 % in KC-C8$^{Fl/Fl}$ mice (Figure 2G, H). In line with this, KC-C8$^{Fl/Fl}$ mice showed a significant increase in overall survival in comparison to KC-C8$^{Fl/Fl}$; MLKL$^{-/-}$ (Figure S3D). Moreover, we found that heterozygous KC-C8$^{WT/Fl}$ mice which have reduced extrinsic apoptotic activity but retain caspase 8-mediated blockade of necroptosis [5,39] show an exacerbated disease phenotype reminiscent of KC-C8$^{Fl/Fl}$; MLKL$^{-/-}$ mice (Figure S3E, F). These data suggest that pancreatic cancer metastases are constitutively edited via the necroptosis and apoptosis pathways.

In contrast to our results using MLKL-deficient mice, a previous study has shown that whole body RIPK3-deficiency in KC-mice ameliorates PanIN progression [40]. Based upon these data it was concluded that necroptosis-associated inflammation promotes pancreatic oncogenesis. In order to account for this discrepancy, we also crossed KC-mice to RIPK3$^{-/-}$ mice [41] and could confirm the prior observed phenotype amelioration in this model (Figure S3E, F). Yet, genetic evidence from mice supports a concept wherein RIPK3 fulfils additional pro-inflammatory functions also within the immune compartment which likely accounts for tumor promotion and extend beyond induction of necroptosis while MLKL-deficiency specifically abrogates necroptosis in mouse models of tissue injury [42]. Moreover, RIPK3 has been shown to limit RIPK1/caspase 8-dependent apoptosis [41,43] and small molecule inhibitors against RIPK3 can trigger apoptosis [44]. To test whether expression of oncogenic KRAS in a minimal cellular system was sufficient to sensitize to apoptosis upon RIPK3 inhibition made possible by elevated caspase 8 expression, we made use of Rasless MEFs (N- and HRAS-deficient MEFs [45]) reconstituted with stable expression of either WT KRAS or KRAS^{G12D} [46]. Indeed, MEFs

expressing $KRAS^{G12D}$ were sensitized to toxicity induced by RIPK3 inhibition (RIPK3i) alone and also to apoptosis induced by TNF, smac mimetic (SM) and RIPK3i, which was entirely reverted by co-incubation with the caspase inhibitor Emricasan indicating the induction of apoptosis in KRAS-mutated cells (Figure S3G). Given that we found that caspase 8 expression is highest within ductal cells amongst non-immune cells and we found that caspase 8-mediated extrinsic apoptosis and necroptosis constitutively limit tumor progression and metastasis in this model, the effects observed with RIPK3-deficiency in PDAC likely relate to impaired inflammatory signaling in immune cells.

Taken together, we provide genetic proof that elevated caspase 8 expression protects pancreatic neoplasia from aberrant anti-tumor necroptosis. Moreover, our data reveal a previously unrecognized constitutive anti-metastatic surveillance via necroptosis and extrinsic apoptosis in pancreatic neoplasia.

Oncogenic KRAS upregulates necroptosis pathway components as part of a type I interferon response

Having found that KRAS-expressing PanINs showed upregulation of caspase 8 (Figure 1) to protect themselves from aberrant necroptosis (Figure 2), we hypothesized that caspase 8 upregulation may be a result of stochastic selection over time whereupon cellular clones with high caspase 8 expression would survive necroptosis leading to a gradual passive upregulation within PanINs. Strikingly, caspase 8 upregulation observed within PanINs in KC-$C8^{WT/WT}$ mice was not evident in KC- $C8^{WT/WT}$;$MLKL^{-/-}$ lesions (Figure 3A) providing genetic evidence for constitutive necroptosis to select for caspase 8^{high} malignant cells. Therefore, we next aimed to understand whether KRAS-expressing cells may have a propensity to undergo cycles of constitutive selection via necroptosis. To first mechanistically address this question in a simplified cellular system which has not undergone intratumoral selection (such as human PDAC cell lines), we generated mouse embryonic fibroblasts (MEFs) from a cross of an inducible Cre strain (CAG-ERT2-Cre) with the LsL-$KRAS^{G12D}$ mouse strain and mTmG reporter mice as previously described [46] (hereafter referred to as LsL-$KRAS^{G12D}$ MEFs). Upon treatment with 4-hydroxytamoxifen (4OHT), tdTomato+ MEFs switched to express GFP indicating successful Cre-mediated recombination and $KRAS^{G12D}$ expression (Figure S4A). Next, we subjected LsL-$KRAS^{G12D}$ MEFs derived from 7 independent embryos from 3 distinct litters to treatment with or without 4OHT and bulk RNA-sequencing in order to obtain information on transcriptional programs imminently induced upon expression of $KRAS^{G12D}$

from its endogenous promotor. Expression of endogenous $KRAS^{G12D}$ most strongly induced a list of *bona fide* interferon-stimulated genes (ISGs) including IRF7, Oas1a, Ccl5, ZBP1, Mx1 and Ifi206 (Figure 3B). Moreover, gene set enrichment analysis (GSEA) confirmed a strong enrichment of type I and II interferon pathway activation along with NF-kB activation, IL-6/STAT3 and KRAS signaling activation signatures (Figure 3C). In line with a proposed mechanism of in vivo selection over time, caspase 8 merely showed a slight upregulation upon direct induction of $KRAS^{G12D}$ (Figure S4B) suggesting that expression of oncogenic KRAS itself may create selective pressure via the necroptosis pathway. Strikingly, induction of $KRAS^{G12D}$ led to an upregulation of MLKL and RIPK3 along with the known KRAS effector pathway target gene DUSP6 (Figure 3D, Figure S4C). Caspase 8 was also very slightly induced. Moreover, in an independent dataset and cellular system comparing Rasless MEFs (N- and HRAS-deficient MEFs [45]) reconstituted with near-endogenous level expression of either WT KRAS or $KRAS^{G12D}$ [46], we also found an enrichment of interferon-related signatures and RIPK3, MLKL to be upregulated in cells constitutively expressing $KRAS^{G12D}$ (Figure S4D, E). To validate a connection of oncogenic KRAS-induced transcriptional activity with IFN pathway activity and ensuing necroptosis pathway upregulation in human PDAC, we computed an ISG score from 11075 patient samples across all cancer types present within the TCGA based upon a published set of 38 ISGs [47] and correlated it with the respective Ras84 score. Indeed, most $Ras84^{high}$ cancer entities also scored high in ISG score (Figure 3E). Moreover, pan-cancer analysis separating high, intermediate and low ISG score cases revealed an almost perfect correlation with the necroptosis molecular machinery as well as caspase 8 (Figure 3F). Indeed, inducible expression of $KRAS^{G12D}$ in normal human pancreatic duct epithelial (HPDE) cells and in KRAS WT human PDAC cell line Bxpc3 and could confirm induction of DUSP6 along with a significant induction of MLKL while induction of caspase 8 was also not detected (Figure S4F, G). To determine the mechanisms of KRAS-induced upregulation of necroptosis pathway components, we next induced $KRAS^{G12D}$ expression in the presence or absence of small molecule inhibitors against the main KRAS effector pathways including the MAPK and AKT pathways and included an inhibitor against Jak1/Jak2 (Ruxolitinib) -known effector kinases inducing ISG expression- in order to address a potential role of the IFN pathway signatures observed in the GSEA analysis. Induction of $KRAS^{G12D}$ expression indeed enhanced total and phosphorylated STAT1 along with a mild induction of ERK and AKT phosphorylation (Figure 3G). Interestingly, inhibition of both the MAPK pathway and the JAK1/2 pathway using Ruxolitinib blocked KRAS-mediated induction of MLKL as well as caspase 8 (Figure 3G). Moreover, this observation could be validated on mRNA level (Figure

S4H). Importantly, siRNA-mediated silencing of JAK1 but not JAK2 was sufficient to abrogate $KRAS^{G12D}$-induced upregulation of MLKL (Figure S4I). JAK1 can activate ISG expression downstream of type I IFN receptor 1 (IFNAR1) and 2 (IFNAR2) upon binding of secreted type I interferons. Therefore, we next tested whether supernatants collected from $KRAS^{G12D}$-uninduced as compared to -induced cells might be sufficient to stimulate expression of the necroptosis machinery in recipient WT and *Ifnar1*$^{-/-}$ MEFs cells lacking the LsL-$KRAS^{G12D}$ locus (Figure 3H). Indeed, supernatants from $KRAS^{G12D}$-induced cells stimulated expression of MLKL in WT but not *Ifnar1*$^{-/-}$ MEFs (Figure 3I). Of note, DUSP6 was, as expected, not induced in these cells given that they did not express oncogenic KRAS. These data strongly suggested supernatants to contain type I interferon activity induced as a result of $KRAS^{G12D}$ expression. Cell autonomous induction of a type I IFN response as well as STAT1 activation has been described to depend upon activation of stimulator of interferon genes (STING) [48]. Indeed, incubation with a small molecule STING inhibitor (STINGi) readily blocked pSTAT1 and MLKL expression upon $KRAS^{G12D}$ induction (Figure 3J). Moreover, we detected significant levels of secreted IFN-α and -ß but not -γ upon induction of $KRAS^{G12D}$ expression which was blunted upon incubation with STINGi (Figure 3K). This induction was not evident in WT MEFs upon 4OHT-treatment (Figure S4J) and thereby clearly dependent upon oncogenic KRAS. Moreover, recipient WT cells simulated with conditioned media from $KRAS^{G12D}$-induced cells in the presence of + STINGi abrogated the induction of the necroptosis machinery (Figure 3L). In support of a $KRAS^{G12D}$-induced type I IFN response, we also observed increased phosphorylation of STAT1 within $KRAS^{G12D}$-driven PanIN lesions of the KC mouse model (Figure S4K). These data indicate that oncogenic KRAS induces STING-dependent soluble type I IFNs which elicit necroptosis pathway component expression upon IFNAR/Jak1 stimulation.

Oncogenic KRAS-induced necroptotic priming represents a synthetic lethality

Based upon the observation that induction of oncogenic KRAS led to type I IFN-dependent upregulation of necroptosis pathway components, we next assessed whether this would be sufficient to sensitize to experimental induction of necroptotic cell death. Strikingly, inducible expression of $KRAS^{G12D}$ created synthetic lethality to necroptotic cell death induced by TNF/emricasan/smac mimetic (TES) an effect which was reverted by RIPK1 or -3 inhibition (Figure 4A). Addition of an MK2 inhibitor (MK2i) to boost formation of the ripoptosome and thereby enhance necroptosis [49] further sensitized cells expressing oncogenic KRAS and was

only reverted by RIPK1 inhibition (Figure 4A). Moreover, constitutive expression of $KRAS^{G12D}$ was also sufficient to selectively sensitise to necroptotic cell death induced by TNF, CD95L or TRAIL all of which was blockable by Nec1s indicating RIPK1-dependent necroptosis (Figure 4B-D). In addition, TES treatment in $KRAS^{G12D}$-expressing or induced MEFs led to an earlier detection of phosphorylated MLKL and RIPK3-indicative of more efficient induction of necroptosis upon expression of oncogenic KRAS (Figure 4E, Figure S5C). Hence, cells expressing oncogenic KRAS are primed to die via necroptosis due to a KRAS-induced type I IFN response; yet, compensatory selection of caspase 8^{high} cells prevents this from happening, a state we term necroptotic priming.

Unlike MEFs, human cancer cell lines frequently lose RIPK3 expression despite detectable RIPK3 expression in associated primary patient tissue [50]. Indeed, we also observed loss of RIPK3 and variable expression of RIPK1 and MLKL in several human PDAC cell lines (Figure S5A) despite the fact that RIPK3 and MLKL are highly overexpressed in the human PAADs dataset as compared to normal pancreas (Figure S5B). These data suggest that primary cancer tissues may be more susceptible to necroptosis than associated cancer cells lines. Nevertheless, about half of the human PDAC cell lines tested known to highly express TRAIL-receptor 2 [37] showed some level of sensitivity to necroptosis induced by TRAIL in combination with zVAD (Figure 4F, G). Contrary to expectations, the only PDAC cell line expressing KRAS wild type (Bxpc3) was highly sensitive to necroptosis. Yet in accordance with the finding of the ISG score to be decisive for necroptosis pathway regulation, Bxpc3 cells had one of the highest ISG scores (data not shown) and also expressed all components of the necroptosis pathway (Figure S5A). In order to assess necroptotic priming of human PDAC but circumnavigate the problem of RIPK3 loss in human PDAC cell lines, we computed a necroptotic priming score for all human cancers by plotting caspase 8 expression as a function of RIPK3/MLKL/ZBP1 co-expression across TCGA datasets. Strikingly, all cancers with frequent KRAS mutations (red) grouped together as the cancers with highest necroptotic priming score (Figure 4H).

Therefore, we propose a model in which oncogenic KRAS induces a STING-dependent type I IFN response which mediates a state of necroptotic priming kept in check by co-selection for high caspase 8 expression (Figure 4I). Importantly, this state of necroptotic priming creates a synthetic lethality of KRAS-mutated cells via the necroptosis pathway.

Targeting necroptotic priming is an effective therapeutic strategy

To test whether the potential synthetic lethality of necroptotic priming can be targeted therapeutically, we isolated murine ducts from KC-mice (Figure 5A), 3D-cultured them to obtain organoids and treated them with TES and also included MK2i to boost formation of the ripoptosome [49]. In this setting TES alone was insufficient to induce necroptosis yet addition of MK2i rapidly killed KC-organoids which could be reverted by addition of nec1s indicative of RIPK1-driven necroptosis (Figure 5B, C). To next test induction of necroptosis in a KRAS-driven cancer model *in vivo*, we treated 21-week-old KC mice for 4 weeks with either vehicle or combined caspase inhibition with a SMAC mimetic (emricasan/birinapant, ES) (Figure 5D). Strikingly, inducing necroptosis showed a very strong anti-tumor effect achieving a restoration of 50% normal pancreatic ducts and strongly reduced presence of $CK19^+$ area and, as a result, less $CD45^+$-cells (Figure 5E-H). While $CD45^+$ cells relative to residual $CK19^+$ area or $TUNEL^+$ cells were not significantly different between both groups at this time point (Figure S6A-C), we could detect cleaved caspase 3/TUNEL double positive cells in vehicle-treated KC-mice while we observed cases of TUNEL-positive cells which were cleaved caspase 3-negative suggesting the presence of regulated necrosis in emricasan/birinapant-treated KC-mice (Figure S6D). Moreover, KC-mice receiving emricasan/birinapant also presented with elevated pancreatic levels of CCL3 and other M1-type inflammatory chemo- cytokines observed in the context of genetic induction of necroptosis (Figure 5I). A hallmark of many cancers including PDAC is chromosomal instability (CIN) which promotes cancer evolution and aggressiveness. Therefore, we next tested therapeutic efficacy of necroptosis induction in mice expressing LsL-$KRAS^{G12D}$ and LsL-$Trp53^{R172H}$ in the pancreas (KPC mice) which gives rise to highly aggressive metastasizing PDAC with high levels of CIN [51]. Strikingly, therapeutic induction of necroptosis via only 4 weeks of treatment as per protocol approved were sufficient to drastically prolong overall survival of KPC mice (Figure 5J, K). Upon necropsy at experimental endpoint, no significant difference in incidence of liver metastasis between the groups was observed which is not surprising given the fact that ES-treated KPC-mice survived significantly longer and, hence had significantly more time to develop metastasis. These results together with the fact that human cancers with KRAS mutations present with high levels of necroptotic priming (Figure 4H) suggest that pharmacological induction of necroptosis might be an effective therapeutic strategy to target human PDAC, a concept which may extend to other cancers with ISG activation profiles.

Discussion

In this work, we have shown that caspase 8 upregulation is an inherent feature of PDAC, arises from necroptosis selection pressure and protects malignant cells from the potentially deleterious effects of a KRAS-driven type I IFN-driven necroptotic response. We show that necroptotic priming via STING-dependent upregulation of type I IFN signaling constitutes a novel vulnerability in PDAC and possibly other cancers where the IFN pathway is activated through other means [47].

We identify that KRAS-induced upregulation of necroptosis pathway components is mediated via induction of a type I IFN response. Of note, in the context of inflammation, the core necroptosis pathway machinery has been described to be regulated as part of a transcriptional IFN response including RIPK3 [52], ZBP1 [53,54] and MLKL [55]. While the KRAS-induced soluble type I IFN response may overall serve prosurvival responses and resistance to DNA damage [56] it comes at the cost of high necroptotic priming. In addition, we find that KRAS-induced type I IFN production is STING-dependent, yet how activated KRAS might activate STING remains to be discovered. Of note, PDAC lesions within the KPC mouse model have been shown to present with vast chromosomal instability (CIN) [51]. While the fact that these mice initially expressing hemizygous $p53^{R172H}$ but lose the p53 wild type allele during tumor progression has been used to argue that CIN may select against the remaining wild type allele and hence originate from mutant p53 expression, several early experiments have linked the expression of oncogenes including activated forms of RAS directly to the rapid induction of CIN in a cell-autonomous manner [57–61]. Importantly, the induction of CIN and the resulting accumulation of cytosolic DNA has been shown to induce STING activation and metastasis[62]. Therefore, it is tempting to speculate whether the observed rapid induction of a STING-dependent type I IFN response might derive from KRAS-induced CIN. Aside from the here discovered causal role of oncogenic KRAS itself in driving an IFN response, caspase 8 or FADD deletion were shown to induce ZBP1- expression and -dependent necroptosis through a cGAS/STING-mediated pathway [63]. Along similar lines, absence of caspase 8 may additionally unleash RIPK1/TBK1-dependent induction of an IFN response [64] which may contribute towards the oncogenic KRAS-induced IFN response we observed here upon caspase 8 deletion *in vivo*. However, we find that aside from the IFN response induced by oncogenic KRAS caspase 8 is co-upregulated through selection thereby keeping cells alive but in a necroptotically primed state. Interestingly, therapeutic induction of necroptosis in acute myeloid leukemia (AML), one of the most

necroptotically primed cancers we find (LAML, Figure 4H), was shown to be highly effective [65]. These data suggest that targeting necroptotic priming might represent a therapeutic treatment strategy which is potentially efficacious beyond PDAC.

Large research efforts of recent years have described the existence of several molecular subtypes of PDAC [66–69]. Interestingly, a recent study identified an IFN signature as characteristic feature within a molecular PDAC subtype deriving from ductal cells and defined by hypomethylation of repetitive elements [70]. Moreover, this subtype largely overlapped with the prior described basal-like subtype of PDAC. Of note, the GSEA transcriptional response pattern we observed upon KRAS induction in MEFs strongly overlapped with the GSEA pattern observed within the basal-like PDAC subtype [21,66–69]. Based upon the observation that we found necroptotic priming to be caused by an oncogenic KRAS-induced type I IFN response, we propose that patients with the high IFN signature subtype comprising the basal-like subtype might benefit from therapeutic caspase inhibition combined with IAP inhibition both stabilizing RIPK1-driven necroptosis in the presence of TNF superfamily ligands [71]. Beyond Ras pathway activation, we also found that cancers with high ISG score presented with high necroptotic priming, hence ISG score might be considered as biomarker group to predict necroptosis vulnerability of several additional aggressive human cancer entities beyond PDAC.

Mechanistically, we find that KRAS-induced cells secrete type I IFNs which are responsible for the induction of further downstream ISGs. This opens up the intriguing possibility that aside from an autocrine effect within KRAS-mutated cells, their secretome may elicit a type I IFN response also in bystander cells including cancer-associated fibroblasts (CAFs). Recently, inflammatory CAFs (iCAFs) have been described which present with activation of IFN-related pathways [27,72,73]. Of note, we also find very high expression of all necroptosis pathway components tested including the strong IFN pathway target gene ZBP1 in iCAFs (Fig. 2a). Therefore, the strong therapeutic effect observed with induction of necroptosis using combined emricasan/birinapant in KC and KPC mice may in part also derive from targeting iCAFs along with cancer cells. In addition, this also suggests that even in cases where cancer cells may have disabled the necroptosis pathway -as we have observed in several cases of human PDAC cell lines- therapeutic induction of necroptosis may still elicit a therapeutic response by targeting the tumor microenvironment (TME). In addition to PDAC cells expressing oncogenic KRAS, other cells within the PDAC TME have been shown to express type I IFNs [74], which would similarly prime PDAC tumors for necroptotic cell death. Taken together, this study assigns a

role for elevated caspase 8 expression in PDAC, contributes towards an understanding of oncogene-driven rewiring of regulated cell death and discovers necroptotic priming as novel principle based on which the clinical use of caspase inhibitors and smac mimetics can be tailored towards targeting PDAC and possibly other IFN-pathway activated cancers.

References

1. Varfolomeev, E.E., Schuchmann, M., Luria, V., Chiannilkulchai, N., Beckmann, J.S., Mett, I.L., Rebrikov, D., Brodianski, V.M., Kemper, O.C., Kollet, O., et al. (1998). Targeted Disruption of the Mouse Caspase 8 Gene Ablates Cell Death Induction by the TNF Receptors, Fas/Apo1, and DR3 and Is Lethal Prenatally. Immunity *9*, 267–276. 10.1016/s1074-7613(00)80609-3.

2. Weinlich, R., Oberst, A., Dillon, C.P., Janke, L.J., Milasta, S., Lukens, J.R., Rodriguez, D.A., Gurung, P., Savage, C., Kanneganti, T.D., et al. (2013). Protective Roles for Caspase-8 and cFLIP in Adult Homeostasis. Cell Reports *5*, 340–348. 10.1016/j.celrep.2013.08.045.

3. Schwarzer, R., Jiao, H., Wachsmuth, L., Tresch, A., and Pasparakis, M. (2020). FADD and Caspase-8 Regulate Gut Homeostasis and Inflammation by Controlling MLKL- and GSDMD-Mediated Death of Intestinal Epithelial Cells. Immunity *52*, 978-993.e6. 10.1016/j.immuni.2020.04.002.

4. Alvarez-Diaz, S., Dillon, C.P., Lalaoui, N., Tanzer, M.C., Rodriguez, D.A., Lin, A., Lebois, M., Hakem, R., Josefsson, E.C., O'Reilly, L.A., et al. (2016). The Pseudokinase MLKL and the Kinase RIPK3 Have Distinct Roles in Autoimmune Disease Caused by Loss of Death-Receptor-Induced Apoptosis. Immunity *45*, 513–526. 10.1016/j.immuni.2016.07.016.

5. Kaiser, W.J., Upton, J.W., Long, A.B., Livingston-Rosanoff, D., Daley-Bauer, L.P., Hakem, R., Caspary, T., and Mocarski, E.S. (2011). RIP3 mediates the embryonic lethality of caspase-8-deficient mice. Nature *471*, 368–372.

6. Oberst, A., Dillon, C.P., Weinlich, R., McCormick, L.L., Fitzgerald, P., Pop, C., Hakem, R., Salvesen, G.S., and Green, D.R. (2011). Catalytic activity of the caspase-8–FLIPL complex inhibits RIPK3-dependent necrosis. Nature *471*, 363–367.

7. Bebber, C.M., Thomas, E.S., Stroh, J., Chen, Z., Androulidaki, A., Schmitt, A., Höhne, M.N., Stüker, L., Alves, C. de P., Khonsari, A., et al. (2021). Ferroptosis response segregates small cell lung cancer (SCLC) neuroendocrine subtypes. Nature Communications *12*, 2048–19.

8. Teitz, T., Wei, T., Valentine, M.B., Vanin, E.F., Grenet, J., Valentine, V.A., Behm, F.G., Look, A.T., Lahti, J.M., and Kidd, V.J. (2000). Caspase 8 is deleted or silenced preferentially in childhood neuroblastomas with amplification of MYCN. Nature Medicine *6*, 529–535.

9. Shivapurkar, N., Toyooka, S., Eby, M.T., Huang, C.X., Sathyanarayana, U.G., Cunningham, H.T., Reddy, J.L., Brambilla, E., Takahashi, T., Minna, J.D., et al. (2002). Differential inactivation of caspase-8 in lung cancers. Cancer biology & therapy *1*, 65–69.

10. Belyanskaya, L.L., Ziogas, A., Hopkins-Donaldson, S., Kurtz, S., Simon, H.-U., Stahel, R., and Zangemeister-Wittke, U. (2008). TRAIL-induced survival and proliferation of SCLC cells is mediated

by ERK and dependent on TRAIL-R2/DR5 expression in the absence of caspase-8. Lung cancer (Amsterdam, Netherlands) *60*, 355–365.

11. Stupack, D.G., Teitz, T., Potter, M.D., Mikolon, D., Houghton, P.J., Kidd, V.J., Lahti, J.M., and Cheresh, D.A. (2006). Potentiation of neuroblastoma metastasis by loss of caspase-8. Nature *439*, 95–99. 10.1038/nature04323.

12. Teitz, T., Inoue, M., Valentine, M.B., Zhu, K., Rehg, J.E., Zhao, W., Finkelstein, D., Wang, Y.-D., Johnson, M.D., Calabrese, C., et al. (2013). Th-MYCN Mice with Caspase-8 Deficiency Develop Advanced Neuroblastoma with Bone Marrow Metastasis. Cancer Res *73*, 4086–4097. 10.1158/0008-5472.can-12-2681.

13. Müller, I., Strozyk, E., Schindler, S., Beissert, S., Oo, H.Z., Sauter, T., Lucarelli, P., Raeth, S., Hausser, A., Nakouzi, N.A., et al. (2020). Cancer Cells Employ Nuclear Caspase-8 to Overcome the p53-Dependent G2/M Checkpoint through Cleavage of USP28. Mol Cell *77*, 970-984.e7. 10.1016/j.molcel.2019.12.023.

14. Liedtke, C., Bangen, J., Freimuth, J., Beraza, N., Lambertz, D., Cubero, F.J., Hatting, M., Karlmark, K.R., Streetz, K.L., Krombach, G.A., et al. (2011). Loss of Caspase-8 Protects Mice Against Inflammation-Related Hepatocarcinogenesis but Induces Non-Apoptotic Liver Injury. Gastroenterology *141*, 2176–2187. 10.1053/j.gastro.2011.08.037.

15. Boege, Y., Malehmir, M., Healy, M.E., Bettermann, K., Lorentzen, A., Vucur, M., Ahuja, A.K., Böhm, F., Mertens, J.C., Shimizu, Y., et al. (2017). A Dual Role of Caspase-8 in Triggering and Sensing Proliferation-Associated DNA Damage, a Key Determinant of Liver Cancer Development. Cancer cell *32*, 342-359.e10.

16. Quante, A.S., Ming, C., Rottmann, M., Engel, J., Boeck, S., Heinemann, V., Westphalen, C.B., and Strauch, K. (2016). Projections of cancer incidence and cancer-related deaths in Germany by 2020 and 2030. Cancer Med-us *5*, 2649–2656. 10.1002/cam4.767.

17. Balachandran, V.P., Beatty, G.L., and Dougan, S.K. (2019). Broadening the Impact of Immunotherapy to Pancreatic Cancer: Challenges and Opportunities. Gastroenterology *156*, 2056–2072. 10.1053/j.gastro.2018.12.038.

18. Rahib, L., Smith, B.D., Aizenberg, R., Rosenzweig, A.B., Fleshman, J.M., and Matrisian, L.M. (2014). Projecting Cancer Incidence and Deaths to 2030: The Unexpected Burden of Thyroid, Liver, and Pancreas Cancers in the United States. Cancer Res *74*, 2913–2921. 10.1158/0008-5472.can-14-0155.

19. Janky, R., Binda, M.M., Allemeersch, J., broeck, A.V. den, Govaere, O., Swinnen, J.V., Roskams, T., Aerts, S., and Topal, B. (2016). Prognostic relevance of molecular subtypes and master regulators in pancreatic ductal adenocarcinoma. Bmc Cancer *16*, 632. 10.1186/s12885-016-2540-6.

20. Pei, H., Li, L., Fridley, B.L., Jenkins, G.D., Kalari, K.R., Lingle, W., Petersen, G., Lou, Z., and Wang, L. (2009). FKBP51 Affects Cancer Cell Response to Chemotherapy by Negatively Regulating Akt. Cancer Cell *16*, 259–266. 10.1016/j.ccr.2009.07.016.

21. Cao, L., Huang, C., Zhou, D.C., Hu, Y., Lih, T.M., Savage, S.R., Krug, K., Clark, D.J., Schnaubelt, M., Chen, L., et al. (2021). Proteogenomic characterization of pancreatic ductal adenocarcinoma. Cell *184*, 5031-5052.e26. 10.1016/j.cell.2021.08.023.

22. East, P., Kelly, G.P., Biswas, D., Marani, M., Hancock, D.C., Creasy, T., Sachsenmeier, K., Swanton, C., consortium, Tracer., Downward, J., et al. (2022). RAS oncogenic activity predicts response to chemotherapy and outcome in lung adenocarcinoma. Nat Commun *13*, 5632. 10.1038/s41467-022-33290-0.

23. Hingorani, S.R., Petricoin, E.F., Maitra, A., Rajapakse, V., King, C., Jacobetz, M.A., Ross, S., Conrads, T.P., Veenstra, T.D., Hitt, B.A., et al. (2003). Preinvasive and invasive ductal pancreatic cancer and its early detection in the mouse. Cancer cell *4*, 437–450.

24. Muzumdar, M.D., Tasic, B., Miyamichi, K., Li, L., and Luo, L. (2007). A global double-fluorescent Cre reporter mouse. genesis *45*, 593–605.

25. Ho, W.J., Jaffee, E.M., and Zheng, L. (2020). The tumour microenvironment in pancreatic cancer — clinical challenges and opportunities. Nat Rev Clin Oncol *17*, 527–540. 10.1038/s41571-020-0363-5.

26. Gabitova-Cornell, L., Surumbayeva, A., Peri, S., Franco-Barraza, J., Restifo, D., Weitz, N., Ogier, C., Goldman, A.R., Hartman, T.R., Francescone, R., et al. (2020). Cholesterol Pathway Inhibition Induces TGF-β Signaling to Promote Basal Differentiation in Pancreatic Cancer. Cancer Cell *38*, 567-583.e11. 10.1016/j.ccell.2020.08.015.

27. Biffi, G., Oni, T.E., Spielman, B., Hao, Y., Elyada, E., Park, Y., Preall, J., and Tuveson, D.A. (2018). IL1-Induced JAK/STAT Signaling Is Antagonized by TGFβ to Shape CAF Heterogeneity in Pancreatic Ductal Adenocarcinoma. Cancer Discov *9*, 282–301. 10.1158/2159-8290.cd-18-0710.

28. Dominguez, C.X., Müller, S., Keerthivasan, S., Koeppen, H., Hung, J., Gierke, S., Breart, B., Foreman, O., Bainbridge, T.W., Castiglioni, A., et al. (2020). Single-Cell RNA Sequencing Reveals Stromal Evolution into LRRC15+ Myofibroblasts as a Determinant of Patient Response to Cancer Immunotherapy. Cancer Discov *10*, 232–253. 10.1158/2159-8290.cd-19-0644.

29. Kopp, J.L., von Figura, G., Mayes, E., Liu, F.-F., Dubois, C.L., Morris, J.P., Pan, F.C., Akiyama, H., Wright, C.V.E., Jensen, K., et al. (2012). Identification of Sox9-Dependent Acinar-to-Ductal Reprogramming as the Principal Mechanism for Initiation of Pancreatic Ductal Adenocarcinoma. Cancer Cell *22*, 737–750. 10.1016/j.ccr.2012.10.025.

30. Angelidis, I., Simon, L.M., Fernandez, I.E., Strunz, M., Mayr, C.H., Greiffo, F.R., Tsitsiridis, G., Ansari, M., Graf, E., Strom, T.-M., et al. (2019). An atlas of the aging lung mapped by single cell transcriptomics and deep tissue proteomics. Nat Commun *10*, 963. 10.1038/s41467-019-08831-9.

31. Ng, K.W., Boumelha, J., Enfield, K.S.S., Almagro, J., Cha, H., Pich, O., Karasaki, T., Moore, D.A., Salgado, R., Sivakumar, M., et al. (2023). Antibodies against endogenous retroviruses promote lung cancer immunotherapy. Nature, 1–11. 10.1038/s41586-023-05771-9.

32. Böttcher, J.P., and Sousa, C.R. e (2018). The Role of Type 1 Conventional Dendritic Cells in Cancer Immunity. Trends Cancer *4*, 784–792. 10.1016/j.trecan.2018.09.001.

33. Preston, G.C., and Cantrell, D.A. (2010). Exploring the Biological Role of Kruppel-Like Factor 2 In Cytotoxic T Lymphocytes. Blood *116*, 2783–2783. 10.1182/blood.v116.21.2783.2783.

34. Herrero-Cervera, A., Soehnlein, O., and Kenne, E. (2022). Neutrophils in chronic inflammatory diseases. Cell Mol Immunol *19*, 177–191. 10.1038/s41423-021-00832-3.

554 35. Li, W., Terada, Y., Tyurina, Y.Y., Tyurin, V.A., Bery, A.I., Gauthier, J.M., Higashikubo, R.,
555 Tong, A.Y., Zhou, D., Nunez-Santana, F., et al. (2022). Necroptosis triggers spatially restricted
556 neutrophil-mediated vascular damage during lung ischemia reperfusion injury. Proc National Acad
557 Sci *119*, e2111537119. 10.1073/pnas.2111537119.

558 36. Karstedt, S. von, Montinaro, A., and Walczak, H. (2017). Exploring the TRAILs less travelled:
559 TRAIL in cancer biology and therapy. Nature Publishing Group *17*, 352–366.

560 37. Karstedt, S. von, Conti, A., Nobis, M., Montinaro, A., Hartwig, T., Lemke, J., Legler, K.,
561 Annewanter, F., Campbell, A.D., Taraborrelli, L., et al. (2015). Cancer cell-autonomous TRAIL-R
562 signaling promotes KRAS-driven cancer progression, invasion, and metastasis. Cancer cell *27*, 561–
563 573.

564 38. Sun, L., Wang, H., Wang, Z., He, S., Chen, S., Liao, D., Wang, L., Yan, J., Liu, W., Lei, X., et al.
565 (2012). Mixed Lineage Kinase Domain-like Protein Mediates Necrosis Signaling Downstream of
566 RIP3 Kinase. Cell *148*, 213–227. 10.1016/j.cell.2011.11.031.

567 39. Oberst, A., Dillon, C.P., Weinlich, R., McCormick, L.L., Fitzgerald, P., Pop, C., Hakem, R.,
568 Salvesen, G.S., and Green, D.R. (2011). Catalytic activity of the caspase-8-FLIPL complex inhibits
569 RIPK3-dependent necrosis. Nature *471*, 363–367.

570 40. Seifert, L., Werba, G., Tiwari, S., Ly, N.N.G., Alothman, S., Alqunaibit, D., Avanzi, A., Barilla,
571 R., Daley, D., Greco, S.H., et al. (2016). The necrosome promotes pancreatic oncogenesis via CXCL1
572 and Mincle-induced immune suppression. Nature *532*, 245–249.

573 41. Newton, K., Dugger, D.L., Wickliffe, K.E., Kapoor, N., Almagro, M.C. de, Vucic, D., Komuves,
574 L., Ferrando, R.E., French, D.M., Webster, J., et al. (2014). Activity of Protein Kinase RIPK3
575 Determines Whether Cells Die by Necroptosis or Apoptosis. Science *343*, 1357–1360.
576 10.1126/science.1249361.

577 42. Newton, K., Dugger, D.L., Maltzman, A., Greve, J.M., Hedehus, M., Martin-McNulty, B.,
578 Carano, R.A.D., Cao, T.C., Bruggen, N. van, Bernstein, L., et al. (2016). RIPK3 deficiency or
579 catalytically inactive RIPK1 provides greater benefit than MLKL deficiency in mouse models of
580 inflammation and tissue injury. *23*, 1565–1576.

581 43. Gautheron, J., Vucur, M., Schneider, A.T., Severi, I., Roderburg, C., Roy, S., Bartneck, M.,
582 Schrammen, P., Diaz, M.B., Ehling, J., et al. (2016). The necroptosis-inducing kinase RIPK3 dampens
583 adipose tissue inflammation and glucose intolerance. Nat Commun *7*, 11869. 10.1038/ncomms11869.

584 44. Mandal, P., Berger, S.B., Pillay, S., Moriwaki, K., Huang, C., Guo, H., Lich, J.D., Finger, J.,
585 Kasparcova, V., Votta, B., et al. (2014). RIP3 induces apoptosis independent of pronecrotic kinase
586 activity. Molecular cell *56*, 481–495.

587 45. Drosten, M., Dhawahir, A., Sum, E.Y.M., Urosevic, J., Lechuga, C.G., Esteban, L.M., Castellano,
588 E., Guerra, C., Santos, E., and Barbacid, M. (2010). Genetic analysis of Ras signalling pathways in
589 cell proliferation, migration and survival. The EMBO Journal *29*, 1091–1104.

590 46. Müller, F., Lim, J.K.M., Bebber, C.M., Seidel, E., Tishina, S., Dahlhaus, A., Stroh, J., Beck, J.,
591 Yapici, F.I., Nakayama, K., et al. (2022). Elevated FSP1 protects KRAS-mutated cells from
592 ferroptosis during tumor initiation. Cell Death Differ, 1–15. 10.1038/s41418-022-01096-8.

47. Liu, H., Golji, J., Brodeur, L.K., Chung, F.S., Chen, J.T., deBeaumont, R.S., Bullock, C.P., Jones, M.D., Kerr, G., Li, L., et al. (2019). Tumor-derived IFN triggers chronic pathway agonism and sensitivity to ADAR loss. Nat Med *25*, 95–102. 10.1038/s41591-018-0302-5.

48. Decout, A., Katz, J.D., Venkatraman, S., and Ablasser, A. (2021). The cGAS–STING pathway as a therapeutic target in inflammatory diseases. Nat Rev Immunol *21*, 548–569. 10.1038/s41577-021-00524-z.

49. Jaco, I., Annibaldi, A., Lalaoui, N., Wilson, R., Tenev, T., Laurien, L., Kim, C., Jamal, K., John, S.W., Liccardi, G., et al. (2017). MK2 Phosphorylates RIPK1 to Prevent TNF-Induced Cell Death. Mol Cell *66*, 698-710.e5. 10.1016/j.molcel.2017.05.003.

50. Uzunparmak, B., Gao, M., Lindemann, A., Erikson, K., Wang, L., Lin, E., Frank, S.J., Gleber-Netto, F.O., Zhao, M., Skinner, H.D., et al. (2020). Caspase-8 loss radiosensitizes head and neck squamous cell carcinoma to SMAC mimetic–induced necroptosis. Jci Insight *5*, e139837. 10.1172/jci.insight.139837.

51. Hingorani, S.R., Wang, L., Multani, A.S., Combs, C., Deramaudt, T.B., Hruban, R.H., Rustgi, A.K., Chang, S., and Tuveson, D.A. (2005). Trp53R172H and KrasG12D cooperate to promote chromosomal instability and widely metastatic pancreatic ductal adenocarcinoma in mice. Cancer cell *7*, 469–483.

52. Samarajiwa, S.A., Forster, S., Auchettl, K., and Hertzog, P.J. (2009). INTERFEROME: the database of interferon regulated genes. Nucleic Acids Res *37*, D852–D857. 10.1093/nar/gkn732.

53. Fu, Y., Comella, N., Tognazzi, K., Brown, L.F., Dvorak, H.F., and Kocher, O. (1999). Cloning of DLM-1, a novel gene that is up-regulated in activated macrophages, using RNA differential display. Gene *240*, 157–163. 10.1016/s0378-1119(99)00419-9.

54. Takaoka, A., Wang, Z., Choi, M.K., Yanai, H., Negishi, H., Ban, T., Lu, Y., Miyagishi, M., Kodama, T., Honda, K., et al. (2007). DAI (DLM-1/ZBP1) is a cytosolic DNA sensor and an activator of innate immune response. Nature *448*, 501–505.

55. Knuth, A.-K., Rösler, S., Schenk, B., Kowald, L., Wijk, S.J.L. van, and Fulda, S. (2018). Interferons Transcriptionally Up-Regulate MLKL Expression in Cancer Cells1. Neoplasia New York N Y *21*, 74–81. 10.1016/j.neo.2018.11.002.

56. Cheon, H., Wang, Y., Wightman, S.M., Jackson, M.W., and Stark, G.R. (2023). How cancer cells make and respond to interferon-I. Trends Cancer *9*, 83–92. 10.1016/j.trecan.2022.09.003.

57. Denko, N.C., Giaccia, A.J., Stringer, J.R., and Stambrook, P.J. (1994). The human Ha-ras oncogene induces genomic instability in murine fibroblasts within one cell cycle. Proc National Acad Sci *91*, 5124–5128. 10.1073/pnas.91.11.5124.

58. Saavedra, H.I., Fukasawa, K., Conn, C.W., and Stambrook, P.J. (1999). MAPK Mediates RAS-induced Chromosome Instability*. J Biol Chem *274*, 38083–38090. 10.1074/jbc.274.53.38083.

59. Saavedra, H.I., Knauf, J.A., Shirokawa, J.M., Wang, J., Ouyang, B., Elisei, R., Stambrook, P.J., and Fagin, J.A. (2000). The RAS oncogene induces genomic instability in thyroid PCCL3 cells via the MAPK pathway. Oncogene *19*, 3948–3954. 10.1038/sj.onc.1203723.

60. Knauf, J.A., Ouyang, B., Knudsen, E.S., Fukasawa, K., Babcock, G., and Fagin, J.A. (2006). Oncogenic RAS Induces Accelerated Transition through G2/M and Promotes Defects in the G2 DNA Damage and Mitotic Spindle Checkpoints*. J Biol Chem *281*, 3800–3809. 10.1074/jbc.m511690200.

61. Woo, R.A., and Poon, R.Y.C. (2004). Activated oncogenes promote and cooperate with chromosomal instability for neoplastic transformation. Gene Dev *18*, 1317–1330. 10.1101/gad.1165204.

62. Bakhoum, S.F., Ngo, B., Laughney, A.M., Cavallo, J.-A., Murphy, C.J., Ly, P., Shah, P., Sriram, R.K., Watkins, T.B.K., Taunk, N.K., et al. (2018). Chromosomal instability drives metastasis through a cytosolic DNA response. Nature *553*, 467–472. 10.1038/nature25432.

63. Rodriguez, D.A., Quarato, G., Liedmann, S., Tummers, B., Zhang, T., Guy, C., Crawford, J.C., Palacios, G., Pelletier, S., Kalkavan, H., et al. (2022). Caspase-8 and FADD prevent spontaneous ZBP1 expression and necroptosis. Proc National Acad Sci *119*, e2207240119. 10.1073/pnas.2207240119.

64. Wang, Y., Karki, R., Mall, R., Sharma, B.R., Kalathur, R.C., Lee, S., Kancharana, B., So, M., Combs, K.L., and Kanneganti, T.-D. (2022). Molecular mechanism of RIPK1 and caspase-8 in homeostatic type I interferon production and regulation. Cell Reports *41*, 111434. 10.1016/j.celrep.2022.111434.

65. Brumatti, G., Ma, C., Lalaoui, N., Nguyen, N.-Y., Navarro, M., Tanzer, M.C., Richmond, J., Ghisi, M., Salmon, J.M., Silke, N., et al. (2016). The caspase-8 inhibitor emricasan combines with the SMAC mimetic birinapant to induce necroptosis and treat acute myeloid leukemia. Sci Transl Med *8*, 339ra69. 10.1126/scitranslmed.aad3099.

66. Raphael, B.J., Hruban, R.H., Aguirre, A.J., Moffitt, R.A., Yeh, J.J., Stewart, C., Robertson, A.G., Cherniack, A.D., Gupta, M., Getz, G., et al. (2017). Integrated Genomic Characterization of Pancreatic Ductal Adenocarcinoma. Cancer Cell *32*, 185-203.e13. 10.1016/j.ccell.2017.07.007.

67. Bailey, P., Chang, D.K., Nones, K., Johns, A.L., Patch, A.-M., Gingras, M.-C., Miller, D.K., Christ, A.N., Bruxner, T.J.C., Quinn, M.C., et al. (2016). Genomic analyses identify molecular subtypes of pancreatic cancer. Nature *531*, 47–52. 10.1038/nature16965.

68. Moffitt, R.A., Marayati, R., Flate, E.L., Volmar, K.E., Loeza, S.G.H., Hoadley, K.A., Rashid, N.U., Williams, L.A., Eaton, S.C., Chung, A.H., et al. (2015). Virtual microdissection identifies distinct tumor- and stroma-specific subtypes of pancreatic ductal adenocarcinoma. Nat Genet *47*, 1168–1178. 10.1038/ng.3398.

69. Collisson, E.A., Sadanandam, A., Olson, P., Gibb, W.J., Truitt, M., Gu, S., Cooc, J., Weinkle, J., Kim, G.E., Jakkula, L., et al. (2011). Subtypes of pancreatic ductal adenocarcinoma and their differing responses to therapy. Nat Med *17*, 500–503. 10.1038/nm.2344.

70. Espinet, E., Gu, Z., Imbusch, C.D., Giese, N.A., Büscher, M., Safavi, M., Weisenburger, S., Klein, C., Vogel, V., Falcone, M., et al. (2021). Aggressive PDACs Show Hypomethylation of Repetitive Elements and the Execution of an Intrinsic IFN Program Linked to a Ductal Cell of Origin. Cancer Discov *11*, 638–659. 10.1158/2159-8290.cd-20-1202.

71. Annibaldi, A., John, S.W., Berghe, T.V., Swatek, K.N., Ruan, J., Liccardi, G., Bianchi, K., Elliott, P.R., Choi, S.M., Coillie, S.V., et al. (2018). Ubiquitin-Mediated Regulation of RIPK1 Kinase Activity Independent of IKK and MK2. Mol Cell *69*, 566-580.e5. 10.1016/j.molcel.2018.01.027.

672 72. Elyada, E., Bolisetty, M., Laise, P., Flynn, W.F., Courtois, E.T., Burkhart, R.A., Teinor, J.A.,
673 Belleau, P., Biffi, G., Lucito, M.S., et al. (2019). Cross-Species Single-Cell Analysis of Pancreatic
674 Ductal Adenocarcinoma Reveals Antigen-Presenting Cancer-Associated Fibroblasts. Cancer Discov
675 *9*, 1102–1123. 10.1158/2159-8290.cd-19-0094.

676 73. Öhlund, D., Handly-Santana, A., Biffi, G., Elyada, E., Almeida, A.S., Ponz-Sarvise, M., Corbo,
677 V., Oni, T.E., Hearn, S.A., Lee, E.J., et al. (2017). Distinct populations of inflammatory fibroblasts
678 and myofibroblasts in pancreatic cancer. J Exp Medicine *214*, 579–596. 10.1084/jem.20162024.

679 74. Parker, B.S., Rautela, J., and Hertzog, P.J. (2016). Antitumour actions of interferons: implications
680 for cancer therapy. Nat Rev Cancer *16*, 131–144. 10.1038/nrc.2016.14.

681 75. Beisner, D.R., Ch'en, I.L., Kolla, R.V., Hoffmann, A., and Hedrick, S.M. (2005). Cutting Edge:
682 Innate Immunity Conferred by B Cells Is Regulated by Caspase-8. J Immunol *175*, 3469–3473.
683 10.4049/jimmunol.175.6.3469.

684 76. Körner, L., Wachsmuth, L., Kumari, S., Schwarzwer, R., Jiao, H., and Pasparakis, M. (2023).
685 ZBP1 causes inflammation by inducing RIPK3-mediated necroptosis and RIPK1 kinase activity-
686 independent apoptosis. 10.21203/rs.3.rs-2511750/v1.

687 77. Surumbayeva, A., Kotliar, M., Gabitova-Cornell, L., Kartashov, A., Peri, S., Salomonis, N.,
688 Barski, A., and Astsaturov, I. (2021). Preparation of mouse pancreatic tumor for single-cell RNA
689 sequencing and analysis of the data. Star Protoc *2*, 100989. 10.1016/j.xpro.2021.100989.

690 78. Ewels, P.A., Peltzer, A., Fillinger, S., Patel, H., Alneberg, J., Wilm, A., Garcia, M.U., Tommaso,
691 P.D., and Nahnsen, S. (2020). The nf-core framework for community-curated bioinformatics
692 pipelines. Nat Biotechnol *38*, 276–278. 10.1038/s41587-020-0439-x.

693 79. Tommaso, P.D., Chatzou, M., Floden, E.W., Barja, P.P., Palumbo, E., and Notredame, C. (2017).
694 Nextflow enables reproducible computational workflows. Nat Biotechnol *35*, 316–319.
695 10.1038/nbt.3820.

696 80. Dobin, A., Davis, C.A., Schlesinger, F., Drenkow, J., Zaleski, C., Jha, S., Batut, P., Chaisson, M.,
697 and Gingeras, T.R. (2013). STAR: ultrafast universal RNA-seq aligner. Bioinformatics *29*, 15–21.
698 10.1093/bioinformatics/bts635.

699 81. Patro, R., Duggal, G., Love, M.I., Irizarry, R.A., and Kingsford, C. (2017). Salmon provides fast
700 and bias-aware quantification of transcript expression. Nat Methods *14*, 417–419.
701 10.1038/nmeth.4197.

702 82. Love, M.I., Huber, W., and Anders, S. (2014). Moderated estimation of fold change and
703 dispersion for RNA-seq data with DESeq2. Genome Biol *15*, 550. 10.1186/s13059-014-0550-8.

704 83. Trauzold, A., Siegmund, D., Schniewind, B., Sipos, B., Egberts, J., Zorenkov, D., Emme, D.,
705 Röder, C., Kalthoff, H., and Wajant, H. (2006). TRAIL promotes metastasis of human pancreatic
706 ductal adenocarcinoma. Oncogene *25*, 7434–7439.

707

708 **METHODS AND MATERIALS**

Antibodies The following antibodies for Western Blots were used: pERK (Thr202/Tyr204) (Cell Signaling, 4307 1:1000), ERK (Cell Signaling, 9102 1:1000), pAKT (Ser473) (Cell Signaling, 4060 1:1000), AKT (Cell Signaling, 4691 1:1000), pStat1 (Tyr701) (Cell Signaling, 9167 1:500), Stat1 (Cell Signaling, 14995 1:1000), pMLKL (Ser345) (Cell Signaling, 37333 1:1000), pMLKL (Ser358) (Cell Signaling, 91689 1:1000), MLKL (Millipore, MABC604 1:1000), MLKL (Cell Signaling, 14993 1:1000), pRIPK1 (Ser166) (Cell Signaling, 65746 1:1000), pRIPK1 (Ser321) (Cell Signaling, 83613 1:1000), RIPK1 (Cell Signaling, 3493 1:1000), pRIPK3 (Thr231/Ser232) (Cell Signaling, 91702 1:1000), RIPK3 (Cell Signaling, 15828 1:1000), RIPK3 (Enzo Life Sciences, ADI-905-242 1:1000), ZBP1 (Adipogen, A42342106 1:1000), Caspase 8 (AdipoGen, AG-20B-0057-C050 1:1000), Caspase 8 (Enzo Life Sciences, ALX-804-447-C100 1:1000) ß-Actin (Sigma, A1978, 1:10,000), GAPDH (Cell Signaling, 97166 1:2000); HRP-conjugated secondary antibodies: goat-anti-mouse-HRP (Linaris GmBH, 20400, 1:10,000), goat-anti-rabbit-HRP (Linaris GmBH, 20402, 1:10,000), goat-anti-rat-HRP (Sigma, A9037, 1:10,000). The following antibodies were used for tissue stainings: Cytokeratin 19 (1:100, AHP1846, Bio rad antibodies (discontinued) and TROMA-III from Developmental Studies Hybridoma Bank Iowa University), CD45 (1:100, 14-0451-82, Invitrogen), Caspase 8 (1:200, ALX-804-447-C100, Enzo), cleaved caspase 3 (1:500, 9661, Cell Signaling), pSTAT1 (1:50, 9167, Cell Signaling).

Reagents Birinapant (S7015, sellekchem), Emricasan (HY-10396 , Hölzel), zVAD (BML-P416-0001, ENZO), nec1s (ab221984, Abcam), GSK872 (530389, Millipore), PF-3644022 hydrate (PZ0188, Sigma Aldrich), TRAIL (1121-TL-010/CF, R&D systems), Fas Ligand (6128-SA-025/CF, R&D systems), PD184352 (PZ0181, Sigma Aldrich), MK2206 (S1078, Sellekchem), Ruxolitinib (S1378, Selleckchem), C-178 (S6667, Selleckchem), DRAQ7 (424001, Biolegend), Dharmafect I (T-2005-01, Dharmacon), Puromycin (Sigma), Doxycycline hydrochloride (Alfa Aesar), 4-hydroxy-tamoxifen (4OHT) (T5648, Sigma), HBS (Sigma Aldrich), propidium iodide (Sigma), AnnexinV (29005, Biotium), Matrigel (Growth Factor Reduced, Phenol Red Free; 356231, Corning), PancreaCult™ Organoid Growth Medium (06040, Stemcell).

Mice LsL-KRAS^{G12D} [23], LsL-Trp53^{R172H} and PDX-Cre mice were purchased from the Jackson Laboratory. Casp8$^{FL/FL}$ mice[75] on a C57BL/6 background were obtained under a material transfer agreement (MTA) from Stephen Hedrick. MLKL$^{-/-}$ mice were newly generated in the

Pasparakis lab and described in Körner et al.[76], RIPK3$^{-/-}$ mice were obtained from Genentech under an existing MTA as part of the Pasparakis lab[41]. All mice were maintained on a 12-hour light/dark cycle with water and food *ad libitum*. For four consecutive weeks, 5-months-old mice were injected i.p. 2 x per week either with vehicle (PBS with 40% PEG-4000, 0.4% DMSO) or Emricasan [2.5 mg/kg] with Birinapant [5 mg/kg]. KC mice were sacrificed four weeks after the last treatment and the pathologist was blinded to the group allocation while performing the progression analysis. 8-week-old KPC mice were treated as described above and kept until humane end point.

Pathological Inspection and quantification of PanINs All Samples were fixed in 4% buffered formalin for a minimum of 24 hours and a maximum of 72 hours, then transferred to paraffin. Three micrometer thin sections were prepared according to the standardized procedures at the Institute of Pathology and hematoxylin-eosin stained (H&E). A histopathologist with particular experience in the field of gastroenteropathology (AQ) evaluated all sections in a blinded manner. All primary ductal structures were identified and their various forms of intraepithelial Neoplasia of the pancreas (PanIN). PanINs were determined according to the current WHO classification (2019) and classified into low grade pancreatic intraepithlial neoplasia versus high grade pancreatic intraepithlial neoplasia. The extent of the PanINs relative to the total of available ductules was also quantified. The majority of the low grade PanINs found corresponded to the classic, simple mucin-filled columnar cells that completely or partially replaced the ductal epithelia. Furthermore, other histomorphological changes were determined: a) duct ectasia b) periductular fibrosis/stroma reaction c) extent and type of inflammation (low versus marked inflammation) (lymphocyte-dominated versus neutrophil-granulocyte dominated inflammation) d) invasive carcinoma.

FACS analysis on pancreatic immune cell infiltrates In order to isolate immune cells from the pancreas, whole tissue was dissected and minced with scalpels into fragments small enough to be aspirated into a 5 ml pipette at RT. 45 ml of tissue suspension was incubated with 5ml of a 10x Triple Enzyme Mix (1 g Collagenase IV, 100 mg Hyaluronidase and 20,000 Units DNase IV into 80 ml HBSS) at RT for 30min on a shaker at 80 rpm. Cell suspension was repeatedly pipetted to further dissociate cells, centrifuged at 50 *x g* at RT for 10 min and the supernatant was collected by passing it through a 70 µm nylon strainer. The bigger pellets at the bottom of the tube were then discarded and the filtered supernatant was centrifuged at 200 *x g* for 5 min. Cell pellets were washed with 10 ml Wash Buffer (1 g BSA and 2 ml 0.5 M EDTA in 800 ml

HBSS) at 200 *x g* for 5 min once and were resuspended with 2 ml ACK lysis buffer (Gibco) for 1 min to deplete red blood cells. Cells were washed with PBS and immediately stained for live/dead cells using the viability dye eFluor660 (eBioscience) (1:1000) in PBS for 30 min, at 4 °C. Cells were then washed twice with FACS buffer (PBS, 2% FCS) and Fc block (CD16/32, biolegend, 1:50) was used 15 min. Cells were then stained with CD45-BV421 (30.F11) or CD45-FITC (30.F11) (biolegend), NK1.1- BV421 (PK136) (biolegend), CD4-V450 (RM4-5) (BD Horizon), CD11b-PE (M1/70) (ebioscience), CD8-PE (53-6.7) (biolegend), CD19- PE (1D3) (ebioscience), CD11c-BV421 (N418) (biolegend), Ly-6G/Ly-6C-FITC (RB6-BC5) (ebioscience) all at 1:1000 for another 30min, at 4°C. For subsequent intracellular stainings, cell pellets were resuspended in 200 µl Fixation/Permeabilization buffer (eBioscience) and incubated overnight at 4 °C. The next day, cells were washed with 1× permeabilisation buffer (eBioscience) and incubated for 15 min with 2% goat serum before adding CD206-BV421 (MMR) (C068C2) or Rat IgG2a, κ-isotype Ctrl -BV-421 (RTK-2758) (biolegend)1:50 for 30 min at 4 °C in 1× permeabilisation buffer. After washing twice with 1× permeabilisation buffer cells were resuspended in FACS buffer. Measurements were acquired using a BD LSR Fortessa flow cytometer and data were analyzed using the FlowJo (10.6.1) software.

Single-cell sample preparation for scRNA-seq and fluorescent cell sorting Mouse pancreata harvested from 5 months-old mice was cut into ~3mm pieces, incubated with 5 ml of digestion medium (200mg/l Dispase (17105041, Thermo Fisher), 200mg/l collagenase P (11249002001, Merck) in DMEM (Gibco) containing Pen/Strep and 1% FCS) for 20 min 37 °C while shaking at 150 rpm. Tissue was processed with gentleMACS™ Octo Dissociator imp.tumor3 program. Then cells were strained through a 70µm strainer, spun down at 300 g for 7 minutes. Blood cells were removed with Red Blood Cell Lysis Solution (Milenyi Biotec 130-094-183). Cells were then washed with 0.04% BSA (9048-46-8, Thermo Fisher) in PBS, strained through a 40µm tissue strainer and resuspended in 0.04% BSA in PBS for scRNA-seq. For fluorescent cell sorting, single cells were prepared as described above, washed in PBS and immediately stained for live/dead cells using the viability dye eFluor660 (eBioscience) (1:1000) in PBS for 30 min, at 4 °C. Cells were then washed twice with FACS buffer (PBS, 2% FCS) and incubated with Fc block (CD16/32, biolegend, 1:50) for 15 min. Then cells were stained with CD45-APC-Cy7 (30.F11) (biolegend), washed and $CD45^-$ cells with or without GFP signal were sorted to obtain $KRAS^{G12D}$- or $KRAS^{WT}$-expressing cells, respectively. Cells were spun down at 200g for 5 min and the cell pellet was used for RNA extraction (according to manufacture instructions 740902.10, Macherey Nagel) and further qPCR analysis.

Single cell RNA-sequencing (scRNA-seq) bioinformatic pipeline

Preprocessing Bioinformatics analysis of single-cell RNA sequencing data was conducted as described previsoly[77] using the reproducible Common Workflow Language (CWL) pipelines available on Scientific Data Analysis Platform (SciDAP). Briefly, raw FASTQ files (GEO accession number) were independently mapped to the mm10 (2020-A from July 7, 2020) reference genome by the Cell Ranger Count (version 4.0.0) pipeline. Produced gene expression profiles per sample were aggregated into a single feature-barcode matrix by running Cell Ranger Aggregate (version 4.0.0) pipeline with disabled depth normalization parameter. All other data analysis workflows described below used the Seurat (version 4.1.0) R package.

Low quality cell removal Low quality cells were removed in two iterations. First, the following filtering thresholds were applied per cell – from 80 to 6000 genes, minimum 500 uniquely mapped fragments, maximum 5 percent of transcripts mapped to mitochondrial genes. Preliminary filtered data were run through the dimensionality reduction pipeline to integrate all samples into a single UMAP. The latter allowed us to identify the red blood cells based on the expression of the marker genes (gene names) and manually exclude them on the next iteration of the filtering pipeline.

Datasets integration and clustering High quality cells from all samples were first processed by dimensionality reduction pipeline. On this step gene expression data from each sample were normalized and scaled using SCTransform function. When scaling, the expression levels of the following genes – Xist and Ddx3y, were set as variables to regress out. Normalized data were then integrated following the instructions from the official Seurat vignette using the first 20 dimensions for principal component analysis (PCA) and UMAP projection. Next, cluster analysis workflow was run on the PCA reduced data using 20 dimensions and 0.1 clustering resolution. Gene markers were identified for each cluster using FindAllMarkers function with default parameters, but returning only upregulated genes. Based on the identified gene markers the cell types were assigned. For the analysis of only immune cells, dimensionality reduction and clustering pipelines were run on the prefiltered cells using 0.2 clustering resolution.

Pseudobulk differential gene expression analysis To identify differences in gene expression profiles between two groups of samples (KC-C8$^{WT/WT}$ and KC-C8$^{Fl/Fl}$) pseudobulk differential gene expression pipeline was run for each identified cell type. Cells were first prefiltered to belong only to the specific cell type, then aggregated to a pseudobulk form within each sample.

Ribosomal, mitochondrial, as well as Xist and Ddx3y genes were excluded from the analysis. Aggregated raw reads counts were processed by DESeq2 as bulk RNA sequencing data. The results were filtered to include only differentially expressed genes with p adjusted values not bigger that 0.05.

Cells LsL-KRAS^{G12D} inducible MEFs were generated as described previously[46]. "Rasless" MEFs reconstituted with either WT KRAS4B or KRAS^{G12D} (RPZ25854, RPZ26198) were generated and kindly provided by the RAS Initiative at the Frederick National Laboratory for Cancer Research (FNLCR), US. Rasless MEFs were grown in Dulbecco's modified Eagle's (DMEM) + GlutaMAX™ medium (Gibco) with 4 µg/ml of blasticidin. Freshly isolated LsL-KRAS^{G12D} inducible MEFs and IFNAR1$^{-/-}$ MEFs were cultured in DMEM (Gibco) supplied with 1% L-Glutamine (Sigma) and 1% Sodium Pyruvate (Sigma). Inducible human pancreatic duct epithelial cells (HPDE) pCW-KRAS^{G12D} were described previously[46] and cultured in 75% RPMI 1640/ medium in presence of 25% keratinocyte growth medium 2 (PromoCell) + 0,5µg Puromycin, Bxpc3 pCW-KRAS^{G12D46} in RPMI 1640 GlutaMAX™ + 1% Sodium Pyruvate (Sigma) + 2,5 µg Puromycin. Human PDAC cell lines BxPC3, A818-6, HPFA2, Capan1, AsPc1, PancTul, Colo357, Capan 2, Panc1, Panc89, MiaPaCa2, PT45 were cultured in RPMI 1640 GlutaMAX™ + 1% Sodium Pyruvate (Sigma). KC- organoids were isolated from KC- mice and cultured as described previously[46]. All media were supplemented with 10% fetal calf serum (FCS) (Sigma Aldrich) and 1000 U/mL of both penicillin and streptomycin (Pen/Strep) (Sigma Aldrich). All cells were kept at 37 °C with 5% CO_2 and tested for mycoplasma at regular intervals (mycoplasma barcodes, Eurofins Genomics).

siRNA transfections

Two hundred microliters Opti-MEM (Gibco) and 1.5 µL Dharmafect Reagent I (Dharmacon) were mixed and incubated for 5–10 min at room temperature. 2.8 µL of siRNA (Stock 20 mM) (Dharmacon) were added to the mixture and incubated for another 30 min at room temperature. After incubation, 200 µL of the mixture was added to each well (6-well) plate and cells were plated on top. Knockdowns were incubated for 72 h, as indicated.

Quantitative real-time PCR (qPCR) The NucleoSpin RNA kit (740955.5, Macherey-Nagel) was used to isolate total RNA following the manufacturer's instructions. The isolated RNA was then converted to cDNA using the LunaScript RT SuperMix Kit (E3010L, New England Biolabs). For qPCR each reaction contained 5 µl of Luna Universal qPCR Master Mix

(M3003E, New England Biolabs), 2 µl of nuclease-free water, 1 µl (10 µM) of primer mix (forward and reverse primers), and 2 µl of cDNA (10 ng/µl). qPCR was performed in quadruplicates on the Quant Studio5 qRT PCR cycler. All results were normalized to the expression of the housekeeping gene control Rpl13a. Primer sequences used can be found in Extended Data Table 1.

Bulk RNA-seq analysis The RNA -seq dataset was analyzed on the CHEOPS HPC cluster of the University of Cologne using the RNA-Seq pipeline of the nf-core suite v3.7[78] with default parameters and Nextflow v21.10.6[79]. For instance, the reads were aligned to the mm10 reference genome sequence using STAR v2.7.10a[80] with default parameters. In the quantification step, reads were counted with the quasi-mapping quantification tool Salmon v1.5.2[81]. Differential expression analysis (DEA) was then performed in R using the DESeq function of the DESeq2 v1.36.0 package[82], with default parameters. Genes with absolute value of log2 fold change ≥ 0.56 and adjusted p-value ≤ 0.05 were considered differentially expressed.

Bioinformatic analysis of human TCGA datasets Processed RNA-sequencing data of TCGA patient cohorts was downloaded using the R packages GenomicsDataCommons and TCGAutils on 2023-01-12. Interferon stimulated gene (ISG) expression signatures were calculated using a published approach and Interferon gene set[47]. In brief, to derive Interferon signature scores, median absolute deviation (MAD) Z-scores of log2-transformed and Transcript Per Million (TPM)-normalized mRNA expression values were calculated per gene. The mean of all signature genes' Z-scores per sample was subsequently defined as the ISG score. Categories of high or low ISG score were defined by the mean ISG score +/- 1 standard deviation, remaining samples were considered having medium ISG score and log2-TPM expression of candidate genes compared between groups. For survival analysis of PAncreatic ADenocarcinoma (PAAD), patients were grouped by Caspase 8 expression as low (lowest 10%) or high Caspase 8 (highest 90%). Kaplan-Meier analysis was performed between both groups. Events after 5 years of follow-up were censored to minimize artifacts by competing risks. The Ras84 gene set was downloaded from East et al.[22] and every gene within the gene set was assigned a value corresponding to the rank of its expression level within each sample. For each sample, the Ras84 score is then calculated as the median of the ranks of the 84 genes. For each tumor cohort, the Ras84 score was calculated as the median of the Ras84 scores of individual samples. The necroptosis score was calculated as the sum of the expression levels

of MLKL, RIPK3, and ZBP1 after log10(TPM+1) transformation. For each tumor cohort, the necroptosis score was calculated as the median of the necroptosis score of individual samples. Mutation data was downloaded from the TCGA repository on 2023-05-03 and cohorts with a frequency of missense mutations in KRAS greater than 25% were marked as high-frequency KRAS tumor types.

Cell death assays (flow cytometry) Four days before treatment 120,000 LsL-KRAS^{G12D} inducible MEFs (with or without 4OHT [1 µg/ml]), one day before treatment 500,000 cells ("Rasless" MEFs) were plated in each well of a 6-well plate. To determine cell death, adherent and detached cells were harvested and stained with propidium iodide (PI) [1 µg/ml] (Sigma Aldrich) or with Fixable Viability Dye eFluor™ 660 (eBioscience™) [1:1000] in PBS (Thermo Fisher) supplemented with 2% FBS. For staining with Annexin V (Biotium) [1 µg/ml] we used manufacturer's protocol. Staining-positive cells were quantified by flow cytometry using an LSR-FACS Fortessa (BD Bioscience) and FlowJo software (BD Bioscience).

Cytotoxicity/viability assay NYONE®

The cells were seeded at 1×10^4 cells/well in 96-well plates. After 24 h, the cells were pre-treated with Birinapant (1 µM; Selleck Chemicals, Houston, Texas, United States) or Birinapant (1 µM) and zVAD-fmk (20 µM, Bachem Holding, Bubendorf, Switzerland) for 1 h, followed by treatment with 100 ng/ml TRAIL (PeproTech, Hamburg, Germany). After 24 h cell viability and cell death were assessed by triple-fluorescence staining with Propidium Iodide (PI) (10 µg/ml, Invitrogen, Karlsruhe, Germany), Calcein AM (0.1 µg/ml, BioLegend, San Diego, California, United States) and Hoechst 33342 (2.5 µg/ml, Invitrogen). PI/Calcein AM/Hoechst 33342 staining was performed by diluting the substances in PBS and adding to the wells. The cells were incubated in the dark at 37°C and 5% CO_2 for 20 min and subsequently centrifuged for 5 min at 400 g. Fluorescence imaging was performed by NYONE® SCIENTIFIC (SYNENTEC GmbH, Elmshorn, Germany) and the images were quantified using YT-software® (SYNENTEC GmbH): Cells stained with Hoechst 33342 and Calcein AM were considered living cells, whereas PI stained cells were counted as dead cells due to the loss of membrane integrity.

Crystal violet cell viability assay

The cells were seeded at 1×10^4 cells/well in 96-well plates. After 24 h, the cells were pre-treated with Birinapant (1 µM; Selleck Chemicals, Houston, Texas, United States) or

Birinapant (1 µM) and zVAD-fmk (20 µM, Bachem Holding, Bubendorf, Switzerland) for 1 h, followed by treatment with 100 ng/ml TRAIL (PeproTech, Hamburg, Germany). After 24 h, cell viability was assayed by crystal violet staining as described previously[83]. In brief, the cells were stained with 0.5% crystal violet (Sigma-Aldrich) in 20% MeOH (Carl Roth GmbH + Co. KG, Karlsruhe, Germany), incubated gently shaking for 20 min and thoroughly washed with ddH_2O. After the wells were dried, they were filled with 200 µl of 100% MeOH and incubated for 20 min at room temperature with gentle shaking. Finally, absorption was measured by Tecan Sunrise at 590 nm and reference at 700 nm.

Live cell imaging (IncuCyte) Five thousand ("Rasless" MEFs) per 96-well plate were seeded 24 h in advance. Treatments were added in two parts: "pre-treatment" everything except TNF or TRAIL or Fas Ligand and 30 minutes later cells are treated with ligands. Cells were imaged using the 10× objective within the IncuCyte SX5 live cell imaging system (Sartorius). For dead cell quantification, 100 nM DRAQ7 (Thermofisher) were added to each well. Cells were imaged for indicated timepoints every 2 h. Analysis for confluence, DRAQ7- positive (dead) or was performed using the Software IncuCyte 2021A (Sartorius).

Organoids treatments KC-organoids were seeded for treatment experiments and their viability was analyzed as described previously[46].

Western Blotting. The cells were washed with PBS and lysed with RIPA buffer (89901, Thermo Fisher), which was supplemented with phosphatase and protease inhibitors (Roche). The protein lysate concentrations were determined using the bicinchoninic acid (BCA) protein assay (50000113, Bio-Rad) and subsequently adjusted to the same concentration. Equal amounts of protein were mixed with a final concentration of 1× LDS sample buffer (NP0008, NuPAGE) and DTT (200mM) and then heated to 80 °C for 10 min. The samples were separated via gel electrophoresis and transferred to nitrocellulose membranes (Bio-Rad). The membranes were blocked in PBS with 0.1% Tween 20 (PBST) with 5% BSA (Sigma-Aldrich) for at least 1 h and incubated with primary antibodies overnight at 4°C. After washing with PBST, membranes were incubated with 1:10000 diluted horse radish peroxidase (HRP)-coupled secondary antibodies for at least 1 h at room temperature. After another washing step, bound antibodies were detected using chemiluminescent Amersham ECL Prime Western Blotting Detection Reagent (RPN2235, Cytiva) or SuperSignalTM West Femto Maximum Sensitivity

Substrate (34095, Thermo Fisher). The FUSION Solo S system and software (Vilber) were used to image the membranes.

ELISA CXCL2 (DY452-05, R&D systems), IFN-α (MFNAS0, R&D systems), IFN-ß (DY8234-05, R&D systems), IFN-γ (DY485-05, R&D systems), TNF (DY410-05, R&D systems), Fas ligand (DY526, R&D systems), TRAIL (DY1121, R&D systems) were used following the manufacturer's instructions. Cell culture supernatants and murine pancreatic extracts were analysed after storage at − 80°C. For mouse samples amounts of released protein was normalized to total protein level in the sample measured by DC protein assay kit (774985, Bio-rad). For the IFN-detecting ELISAs, cell culture supernatants were 16-fold concentrated using using 3 kDa molecular weight cut-off spin columns (VS2092, Satorius).

Tissue stainings (immunohistochemistry and immunofluorescence) Pancreatic tissues were fixed in 4% paraformaldehyde, embedded in paraffin and cut into 3–5 µm sections. Paraffin sections were rehydrated by passing the slides through xylene and descending grades of alcohol then rinsed in water. The slides for IHC were incubated for 15 minutes with Peroxidase Blocking Solution (SP-6000, Vector Laboratories). Then heat-induced antigen retrieval was performed in citrate buffer (H-3300, Vector Laboratories) in a pressure cooker (110°C) for 1.5h or by proteinase K treatment for 15 min at 37°C (only CD45). Slides were then immediately cooled under running water and rinsed in PBS. 100 µl of Protein Block (ab64226, Abcam) was added to each slide for 45 minutes. After washing 3 x with 0.05% PBS/Tween 20 solution for 5 minutes, the slides were incubated with 100 µl of the primary antibody at 4°C overnight in a humidity chamber. Following overnight incubation, slides were washed with 0.05% PBS/Tween 20 solution. The sections were then incubated with secondary antibody for 1 h at room temperature and again washed three times. For IHC, the sections were developed using the ABC kit (PK-6100, Biozol) and consequently incubated with DAB substrate before being counterstaining with haematoxylin and rinsed in water for 1 minutes. Slides were then dehydrated in ascending grades of alcohol and cleared in xylene (IHC). Finally, the sections were mounted using Di-N-Butyle Phthalate in Xylene (DPX) mounting solution and covered with a glass coverslip (IHC) or mounted in DAPI (ProLong® Golds antifade reagent with DAPI, Invitrogen) (IF). For negative controls, adjacent duplicate slides from each case were used. These slides were incubated with 100 µl antibody diluent instead of primary antibody/secondary antibody. H&E stainings were examined by an experienced pathologist (A.Q.) who was blinded to the study design. TUNEL stainings were performed according to

manufacturer's protocol (Promega, G3250) for paraffin embedded tissue. The propidium iodide step was omitted, and slides were instead covered with ProLong™ Gold Antifade mounting medium with DAPI (Invitrogen™, P36941). The Trichrome staining was performed according to the manufacturer's protocol of the Trichrome Stain (Masson) Kit (HT15-1KT, Sigma-Aldrich). Fluorescence pictures were acquired using the Keyence BZ-X800 microscope and analyzed with the BZ-X800 Analyzer software. Cytokeratin 19 and CD45 IHC stainings were analyzed and quantified using the QuPath software.

Statistical analysis The data were analyzed by GraphPad Software and either t-test, one-way ANOVA or two-way ANOVA was used to calculate p values as indicated. Results were arranged by the Tukey method and were considered significant at $p < 0.05$. In vitro results and in vivo results are presented as mean ± SEM unless otherwise noted. A minimum of $n \geq 3$ was used for all experiments.

Ethics approval Our study makes use of publicly available TCGA and other cited RNA-sequencing datasets. As such, prior ethics approval has been obtained for these studies and no additional approval is required. All mouse experiments were conducted in accordance with an Institutional Animal Care and Use Committee (IACUC). All people involved in animal experiments received prior training and have passed the additionally required personal licensing course (FELASA B). All animal experiments were approved by the local authorities (LANUV, North-Rhine-Westphalia, Germany).

Data availability

The single cell RNA-seq datasets are available from Sequence Read Archive (SRA) accession code PRJNA975357 and bulk RNA-seq datasets are available on SRA accession code PRJNA975358. Other data are available from the corresponding authors upon reasonable request.

Acknowledgements We thank Christian Reinhardt for advice regarding the LsL-KRAS^{G12D}-mouse strain, Henning Walczak for providing recombinant TRAIL and TNF, Sophie de Carné Trécesson for bioinformatic advice, Dennis Plencker for advice regarding organoid cultures and Nieves Peltzer for helpful discussions. This work was supported by a Max-Eder-Junior Research Group grant (701125509-S.v.K) by the German Cancer Aid, a collaborative research center grant on cell death (SFB1403, A05-S.v.K.) and a PhD student fellowship (S.T.) under Germany's Excellence Strategy – (CECAD, EXC 2030 – 390661388, as part of the Cologne

Graduate School of Aging) both funded by the German Research Foundation (Deutsche Forschungsgesellschaft, DFG), by an eMed consortium grant (01ZX1901A-S.v.K) funded by the German state (BMBF) and a project grant (A07-S.v.K.) funded by the center for molecular medicine (CMMC), Cologne, Germany. S.v.K is receiving funding via CANTAR which is funded through the programme " Netzwerke 2021", an initiative of the Ministry of Culture and Science of the State of Northrhine Westphalia, Germany. The sole responsibility for the content of this publication lies with the authors. J.B. was supported by a Mildred Scheel Nachwuchszentrum Grant 70113307 by the German Cancer Aid.

Author contributions. S.T. performed all in vivo experiments and most in vitro experiments, designed experiments, supervised technical help provided by J. B., L. M., M. M., M. R. and J. S. and co-wrote the manuscript. A. D. performed many mechanistic experiments, A. A. performed FACS analysis of immune cells and helped with project steering, A. T. A., G. G. B., C. M. B., J. K. M. L and J. B. performed bioinformatic analysis on human and murine bulk RNA-seq data, M. K. performed all scRNA-seq data processing and analysis, F. H. performed necroptosis killing experiments in human PDAC cells, H. R.-K performed STING mechanistic experiments, R. M. W. helped with MEF experiments, A. Q. performed pathological inspection and quantification of tissues, A. T., M. P., F. B., G. L., S. B. and I. A. provided important project guidance and input. S.v.K. conceived the project, designed experiments, supervised work, acquired funding and wrote the manuscript. All authors read and edited the manuscript.

Competing interests

The authors declare no conflict of interest.

Correspondence and requests for materials should be addressed to S.v.K.

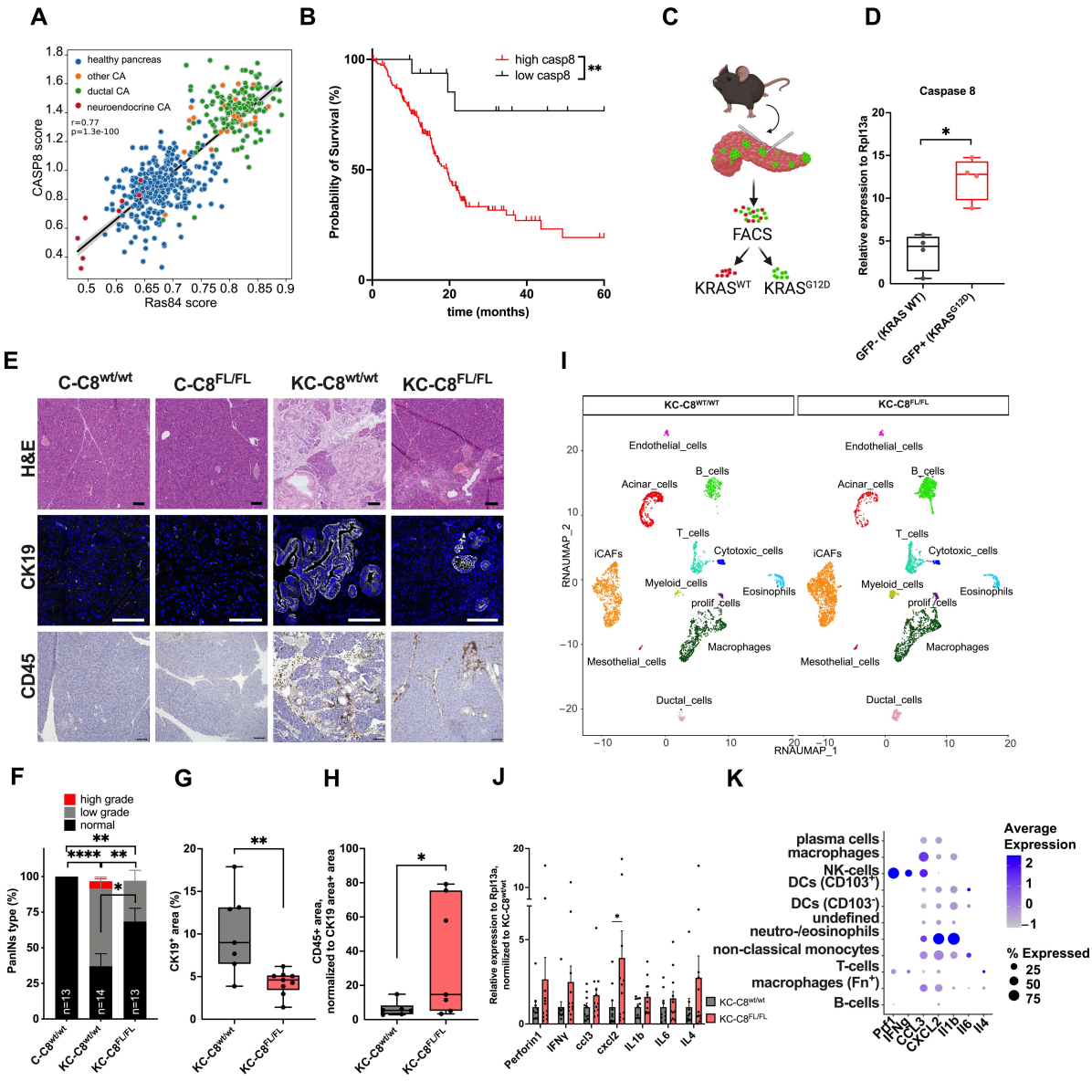

Figure 1. Caspase 8 upregulation protects oncogenic KRAS-driven pancreatic neoplasia

(A) Caspase 8 expression levels are plotted as a function of the Ras84 score[22] in the PAAD TCGA and normal human pancreas (GTEx) datasets.

(B) Kaplan Meier survival of the 10th percentile highest caspase 8 expression vs. the rest within the PAAD dataset (TCGA) is plotted.

(C) Schematic representation of GFP+ and dtTomato+ cell isolation from pancreata of KC-mice.

(D) Caspase 8 mRNA from adjacent WT pancreas (dtTomato+, n=4) and KRASG12D-expressing PanINs (GFP+, n=4) from 5 months-old KC mice was quantified by qPCR. Boxplot center line, mean; box limits, upper and lower quartile; whiskers min. to max.

(E-H) 5 months-old mice of the indicated genotypes were sacrificed and pancreata were excised, fixed and stained by H&E and for CK19 or CD45, (E) representative images are shown. Size bars represent 100 µm. (F) 5 months-old C-C8$^{WT/WT}$ (n=13), KC-C8$^{WT/WT}$ (n=14) and KC-C8$^{FL/FL}$ (n=13) mice were stained by H&E. % of ducts visible per section were graded and quantified by blinded pathological inspection. (G) KC-C8$^{WT/WT}$ (n=7) and KC-C8$^{FL/FL}$ (n=9) sections were stained for CK19 using immunofluorescence and immunohistochemistry and quantified using QuPath. Boxplot center line, mean; box limits, upper and lower quartile; whiskers min. to max. (H) KC-C8$^{WT/WT}$ (n=6) and KC-C8$^{FL/FL}$ (n=7) sections were stained for CD45 using immunohistochemistry, CD45^{+} area normalized to CK19^{+} area was quantified using QuPath. Boxplot center line, mean; box limits, upper and lower quartile; whiskers min. to max.

(I) Single cell suspensions from 5 months-old KC-C8$^{WT/WT}$ (n=3) and KC-C8$^{FL/FL}$ (n=2) were subjected to single cell RNA-sequencing (scRNA-seq) and RNA UMAP plots were generated as indicated.

(J) Pancreata from 5 months-old KC-C8$^{WT/WT}$ (n=10), KC-C8$^{FL/FL}$ (n=13) were isolated and RNA extracted. The indicated cytokines were detected within bulk RNA using qPCR.

(K) Cell type-specific expression of the indicated genes is shown as log1p-transformed scaled average gene expression (scale factor 10000) within CD45^{+} KC-C8$^{WT/WT}$ single cells. Data are means +/- SEM. Two-way ANOVA + Tukey's multiple comparison test (F), Log-rank test for survival analysis (B) and two-tailed unpaired *t* tests for all others, ****p<0.0001, * p<0.05.

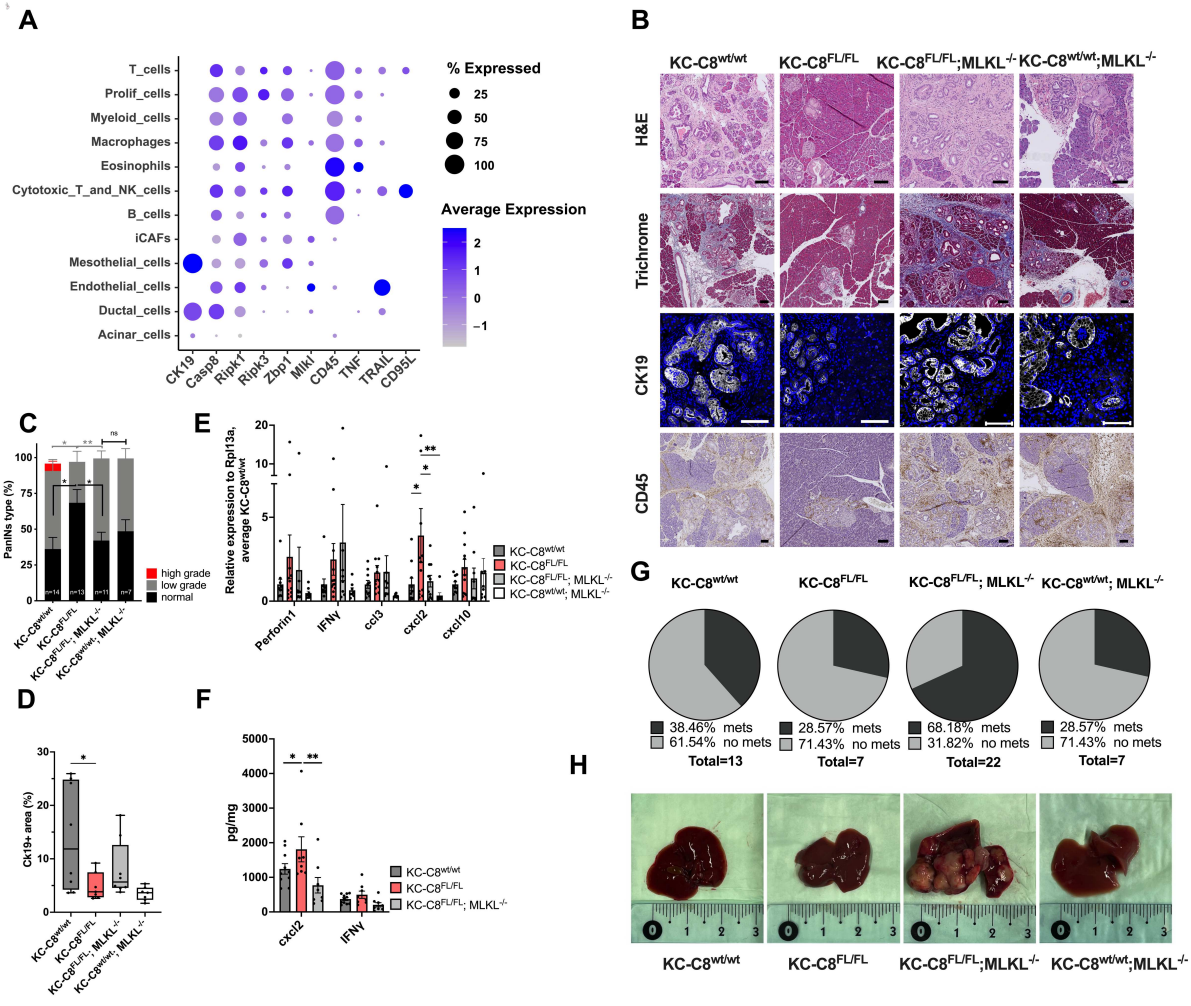

1090

1091 **Figure 2. Pancreatic neoplasia progression is pruned by constitutive necroptosis and**
1092 **apoptosis**

1093 (A) Cell type-specific expression of the indicated genes is shown as log1p-transformed scaled
1094 average gene expression (scale factor 10000) within all KC-C8$^{WT/WT}$ single cells.

1095 (B-D) 5 months-old mice of the indicated genotypes were sacrificed and pancreata were
1096 excised, fixed and stained by H&E, trichrome, CK19 or CD45, (B) representative images are
1097 shown. Size bars represent 100 µm. (C) 5 months-old KC-C8$^{WT/WT}$ (n=14), KC-C8$^{FL/FL}$ (n=13),
1098 KC-C8$^{FL/FL}$;MLKL$^{-/-}$ (n=11) and KC-C8$^{WT/WT}$;MLKL$^{-/-}$ mice (n=7) were stained by H&E. %
1099 of ducts visible per section were graded and quantified by blinded pathological inspection. (D)
1100 Pancreata from 5 months-old KC-C8$^{WT/WT}$ (n=8), KC-C8$^{FL/FL}$ (n=8), KC-C8$^{FL/FL}$;MLKL$^{-/-}$
1101 (n=8) and KC-C8$^{WT/WT}$;MLKL$^{-/-}$ mice (n=7) were stained for CK19 using immunofluorescence
1102 and immunohistochemistry, CK19^{+} area was quantified using QuPath. Boxplot center line,
1103 mean; box limits, upper and lower quartile; whiskers min. to max.

1104 (E) Pancreata from 5 months-old KC-C8$^{WT/WT}$ (n=8), KC-C8$^{FL/FL}$ (n=8), KC-C8$^{FL/FL}$;MLKL$^{-/-}$

(n=8) and KC-C8$^{WT/WT}$;MLKL$^{-/-}$ (n=8) were isolated and RNA extracted. The indicated cytokines were detected within bulk RNA using qPCR.

(F) protein extracts from samples as in e were subjected to ELISA for the quantification of the indicated secreted proteins.

(G) percentage of macroscopic liver metastasis was quantified at experimental endpoint. (H) Photos of representative livers are shown. Data are plotted as means +/- SEM. Two-way ANOVA + Tukey's multiple comparison test (C), Ordinary one-way ANOVA (D) and two-tailed unpaired *t* tests for all others, ****$p<0.0001$, * $p<0.05$.

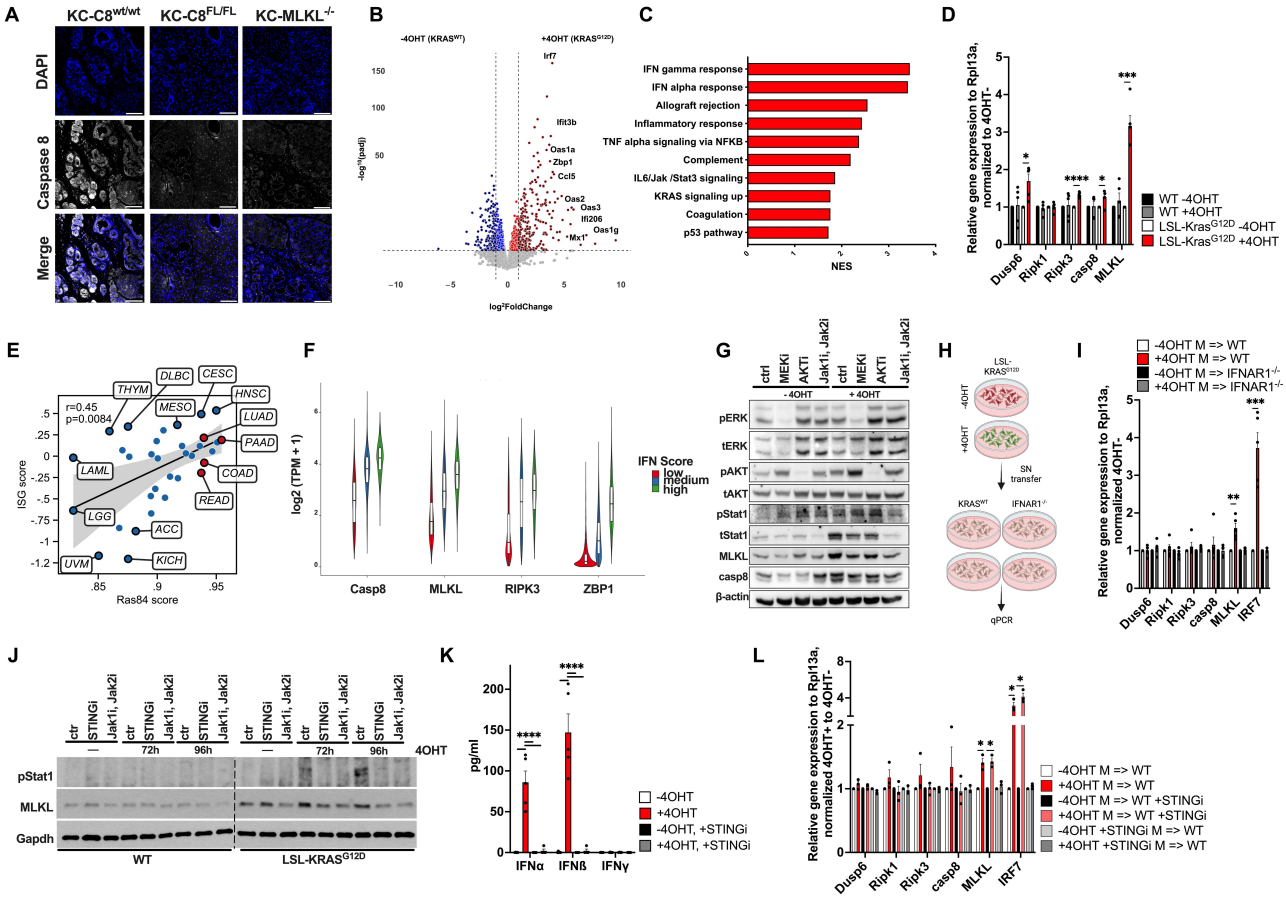

Figure 3. Oncogenic KRAS upregulates necroptosis pathway components as part of a type I interferon response

(A) 5 months-old mice of the indicated genotypes were sacrificed and pancreata were excised, fixed and stained for caspase 8. Representative images are shown. Size bars represent 100 µm.

(B and C) 7 individual LsL-KRAS^{G12D};mTmG MEF lines generated from 3 distinct litters were treated with control or 4OHT [1µM] for 96 h. RNA was collected and sequenced. (B) A volcano plot for the top 20 upregulated transcripts by adjusted p-value [p(adj)] or fold change is shown. red = +4OHT (KRAS^{G12D}), blue= -4OHT (KRAS^{WT}). (C) A ranked list from the RNA-seq data from b was subjected to gene set enrichment analysis (GSEA). Significant negative enrichment score (NES) is shown for all hallmark gene sets within the KRAS^{G12D}-induced group (+4OHT).

(D) Expression of the indicated genes was quantified in qPCR experiments in MEFs detailed in B.

(E) An ISG score was computed as published[47] and correlated to the Ras84 score which was calculated as the median of the ranks of the 84 genes associated with RAS oncogenic activity[22].

Red dots mark cancers with frequent KRAS mutations. (F) Gene expression of Casp8, MLKL, Ripk3 and ZBP1 within cancers with high, intermediate and low ISG score.

(G) LsL-KRAS^{G12D} MEFs as in a were treated with 4OHT [1μM] for 48h and subsequently treated with either MEKi [PD184352, 5μM] or AKTi [MK2260, 5μM] or Jak1/2i [Ruxolitinib, 1μM] for another 48h. The indicated proteins were detected by Western blotting.

(H and I) Schematic representation of supernatant transfer experimental set-up for I. (I) To generate supernatants, LSL-KRAS^{G12D} MEFs were treated with or without 4OHT [1μM] for 36 h to induce KRAS^{G12D}. After this, media were replaced by fresh media without 4OHT and incubated for additional 60 h. Media were collected, spun down and recipient WT or *ifnar1*$^{-/-}$ MEFs were incubated with these supernatants for 60h and mRNA expression of the indicated genes was quantified by qPCR. M; media.

(J) LsL-KRAS^{G12D} or WT (ERT2_Cre) MEFs were treated with control or 4OHT for the indicated times +/- DMSO, STINGi [C-178, 10μM] or Jak1/Jak2i [Ruxolitinib, 1μM]. Representative Western Blots for the indicated proteins are shown.

(K) LSL-KRAS^{G12D} MEFs were treated with or without 4OHT [1μM] for 96 h to induce KRAS^{G12D} +/- STINGi as indicated [C-178, 10μM], followed by 16-fold supernatant concentration using 3 kDa molecular weight cut-off spin columns and supernatants were subjected to ELISA quantification of the indicated proteins.

(L) To generate supernatants, LSL-KRAS^{G12D} MEFs were treated with or without 4OHT [1μM] for 36 h to induce KRAS^{G12D} +/- STINGi as indicated [C-178, 10μM]. After this, media were replaced by fresh media without 4OHT and incubated for additional 60 h. Media were collected, spun down and recipient WT MEFs which did or did not receive STINGi as indicated [C178, 10μM] 2 days prior to supernatant stimulation were then incubated with these supernatants for 60h and mRNA expression of the indicated genes was quantified by qPCR. M; media. Each gene is normalized to its respective non-induced media control stimulation. Data are means +/- SEM or representative images if not indicated otherwise. Two-tailed unpaired t tests, ****$p<0.0001$, ** $p<0.01$.

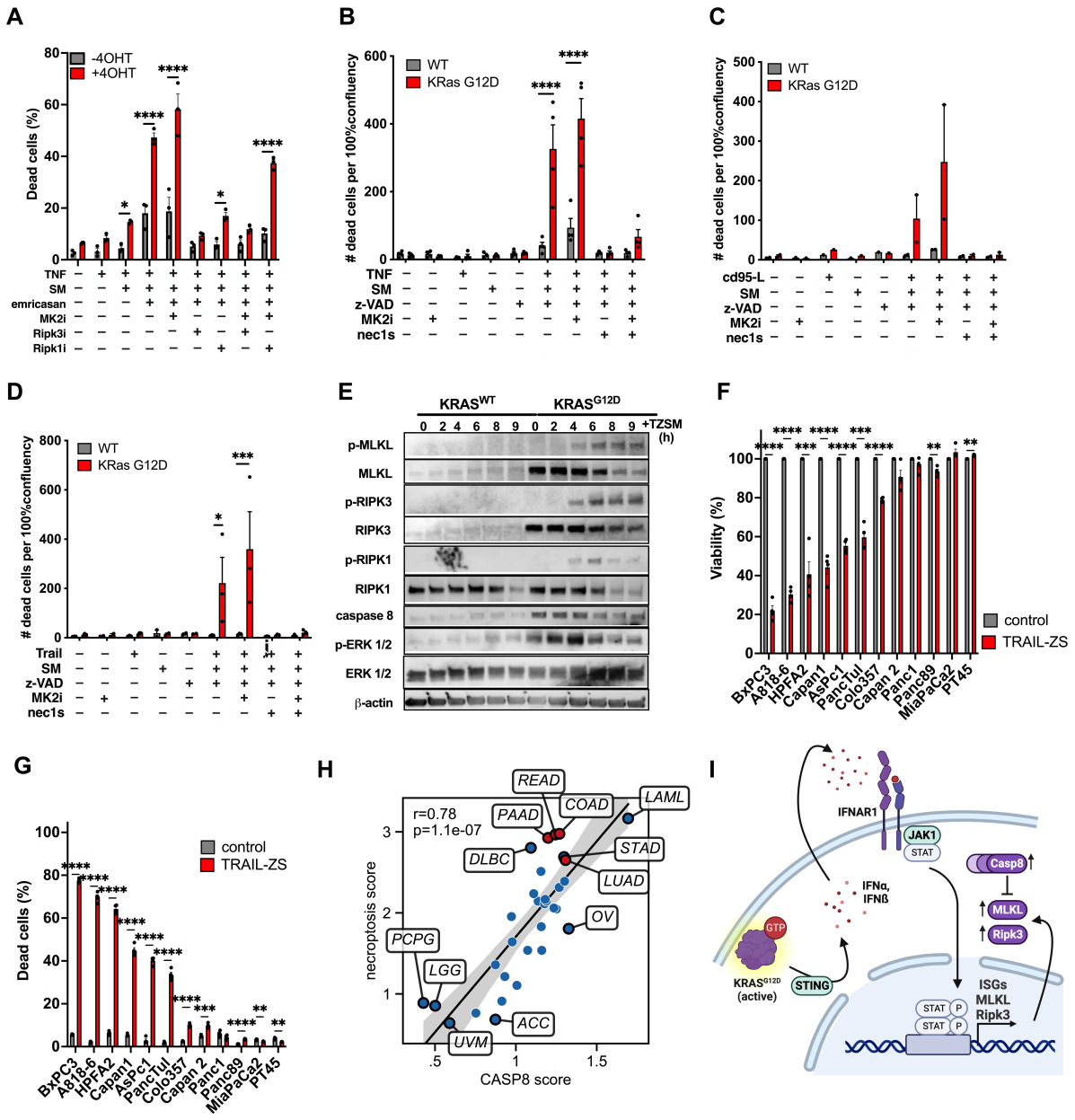

Figure 4. Oncogenic KRAS-induced necroptotic priming represents a synthetic lethality

(A) LsL-KRAS^{G12D} or WT (ERT2_Cre) MEFs were treated with control or 4OHT for 96h followed by the indicated treatment combination for 24h TNF [50ng/ml], SM [1µM], emricasan [2.5µM], MK2i [10µM], RIPK3i [3.3µM] and RIPK1i [10µM]. Dead cells (eFluor660^{+} cells) were quantified by flow cytometry.

(B-D) KRAS^{G12D} and KRAS^{WT} MEFs (Rasless MEFs constitutively reconstituted) were treated with (SM, birinapant [1 µM], z-VAD [20 µM], MK2i [20 µM], nec1s [10 µM], TNF [50 ng/ml], TRAIL [1 µg/ml], CD95-L [1 µg/ml]). Cell death was analyzed by DRAQ7 fluorescence with normalization to cell confluence using the IncuCyte S3 bioimaging platform.

(E) KRAS WT or G12D MEFs (Rasless MEFs constitutively reconstituted) were treated for the indicated times with combined TNF [50ng/ml], SM [1μM], emricasan [2.5μM] and MK2i [10μM]. Representative Western blots are shown.

(F and G) The indicated human PDAC cell lines were treated with the smac mimetic (S) birinapant [1 μM], z-VAD (Z) [20 μM] and TRAIL (T) [100 ng/ml]. (F) Viability was quantified using the crystal violet cell viability assay. (G) Percentage of dead cells from cells treated as in c was analyzed using the NYONE fluorescence assay.

(H) A necroptosis score was computed based upon combined RIPK3, MLKL and ZBP1 expression and correlated to the median caspase 8 expression across all human TCGA datasets. Red dots mark cancers with frequent KRAS mutations.

(I) schematic representation of proposed mechanism. Data are means +/- SEM or representative images if not indicated otherwise. Two-tailed unpaired *t* tests, ****$p<0.0001$, ** $p<0.01$.

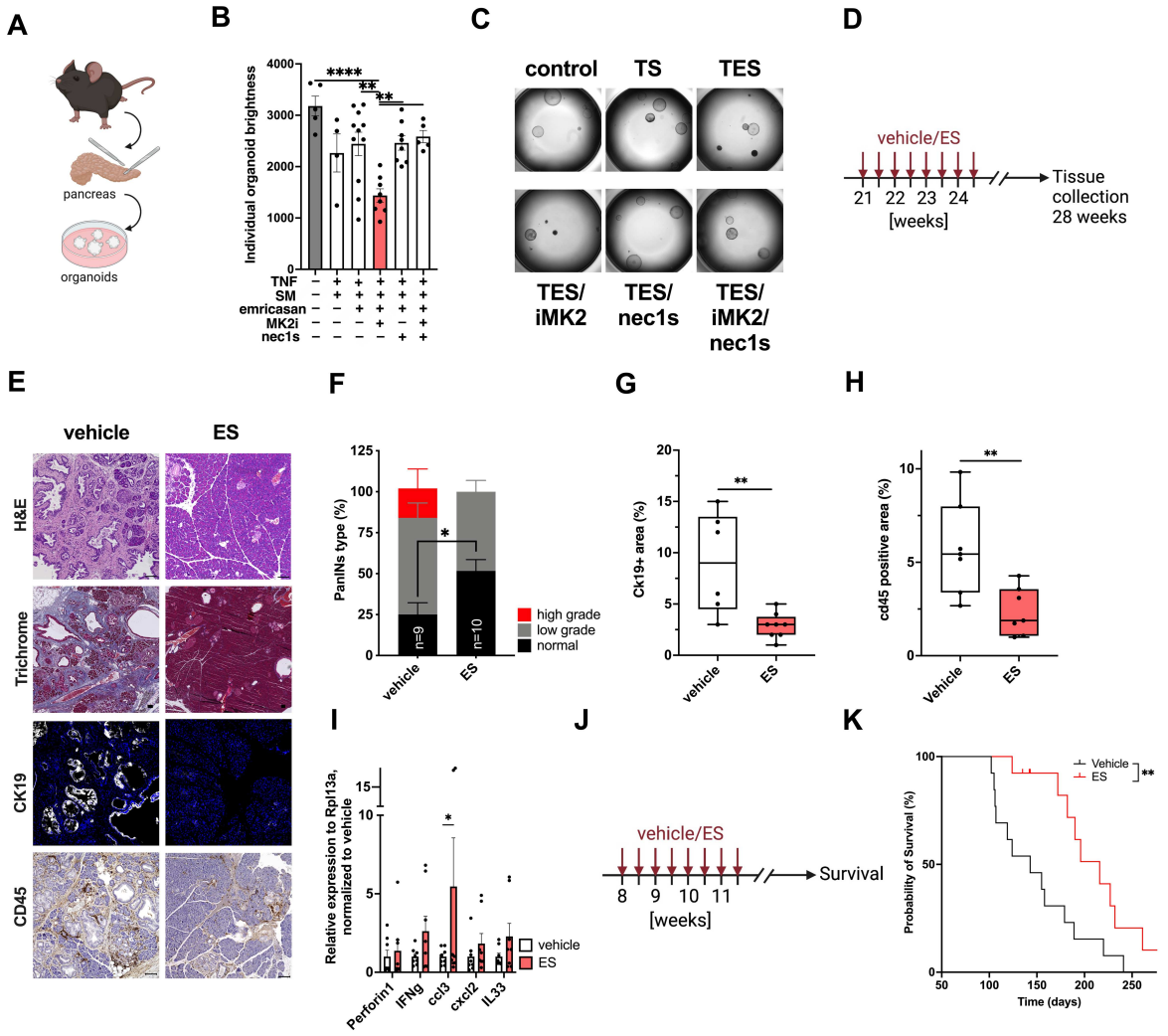

Figure 5. Targeting necroptotic priming is an effective therapeutic strategy

(A) Schematic representation of organoid isolation from KC-mice. (B) organoids were isolated from 5 months-old KC-mice. Once growing, they were dissociated into single cell suspension, counted and seeded +/- the indicated treatments for 24h: TNF [500ng/ml], SM [1μM], emricasan [2.5μM], MK2i [10μM], RIPK3i [3.3μM] and RIPK1i [10μM]. Organoid viability was quantified using organoid brightness as a proxy and the BZ-X800E microscope (Keyence) and BZ-H4M/Measurement Application Software (Keyence). (C) images of representative organoids are show.

(D-I) (D) Scheme of KC-mice treatment schedule. (E) 5 months-old KC-mice were treated i. p. with vehicle (PBS with 40% PEG-4000, 0.4% DMSO) (n=9) or Emricasan (E) [2.5 mg/kg] / Birinapant (smac mimetic; S) [5 mg/kg] (n=10), twice a week for 4 consecutive weeks. Four weeks after the last treatment the mice were sacrificed, pancreata excised and tissues analyzed by the indicated stains. Representative images are shown. (F) in pancreata from treated mice as in d, % of ducts visible per section were graded and quantified by a pathological blinded to

the group allocation. (G) vehicle (n=6) and ES (n=8)-treated sections were stained for CK19 using immunofluorescence and $CK19^+$ area was quantified as before. Boxplot center line, mean; box limits, upper and lower quartile; whiskers min. to max. (H) vehicle (n=7) and ES (n=7)-treated sections were stained for CD45 using immunohistochemistry and $CD45^+$ area was quantified with QuPath. Boxplot center line, mean; box limits, upper and lower quartile; whiskers min. to max. (I) mRNA expression of the indicated genes within bulk pancreatic mRNA extracts from mice treated as in d was quantified using qPCR in vehicle (n=8) and ES (n=8)-treated pancreata.

(J) Scheme of KPC mice treatment schedule. (K) 8-week-old KPC mice were treated with vehicle (PBS with 40% PEG-4000, 0.4% DMSO) (n=14) or the combination of Emricasan [2.5 mg/kg] / Birinapant [5 mg/kg] (n=13), twice a week for 4 consecutive weeks. Mice were kept for Kaplan Meier survival studies until experimental endpoint was met. Data are plotted as means +/- SEM. Two-way ANOVA + Tukey's multiple comparison test (F), Log-rank test for survival analysis (K) and two-tailed unpaired *t* tests for all others, ****$p<0.0001$, * $p<0.05$.

Supplementary Files

This is a list of supplementary files associated with this preprint. Click to download.

- TishinaetalSupplementalfileupdated.pdf